Journal of Materials Chemistry A

REVIEW

View Article Online
View Journal | View Issue

Cite this: J. Mater. Chem. A, 2024, 12, 19606

CO_2-tolerant perovskite cathodes for enhanced solid oxide fuel cells: advancements, challenges, and strategic perspectives

Zilin Ma,[a] Qirui Ye,[a] Huaqing Ye,[a] Feifei Dong, *[ab] Meng Ni *[c] and Zhan Lin [ab]

The key to realizing efficient and durable operation of solid oxide fuel cells (SOFCs) lies in the development of CO_2-tolerant cathodes, a major determinant of the overall power output in the presence of contaminants. Significant strides have been made in recent years toward developing highly CO_2-tolerant perovskite cathodes, forecasting a bright future for SOFCs. This review presents an integrated and comprehensive discussion on this topic, encompassing the latest progress, underlying reaction mechanisms, various evaluation methods, and feasible coping strategies. Particular attention is devoted to cutting-edge characterization technologies, with an emphasis on *in situ*/*operando* characterization tools, together with density functional theory calculations. They are employed to provide an in-depth insight into the complex interactions between electrodes and contaminants, enabling the tailored design of cathode surfaces and interfaces to enhance performance. On this basis, by combining experimental insights with theoretical analysis, this review articulates a comprehensive roadmap for the rational design of state-of-the-art perovskite cathode materials. Ultimately, this advancement is expected to usher in a new generation of fully CO_2-tolerant cathode materials, thereby further bolstering the capability of SOFCs.

Received 9th April 2024
Accepted 25th June 2024

DOI: 10.1039/d4ta02455a

rsc.li/materials-a

[a]Guangdong Provincial Key Laboratory of Plant Resources Biorefinery, School of Chemical Engineering and Light Industry, Guangdong University of Technology, Guangzhou Higher Education Mega Center, Guangzhou 510006, P. R. China. E-mail: dongff@gdut.edu.cn

[b]Jieyang Branch of Chemistry and Chemical Engineering Guangdong Laboratory, Jieyang 515200, P. R. China

[c]Department of Building and Real Estate, Research Institute for Sustainable Urban Development (RISUD) & Research Institute for Smart Energy (RISE), The Hong Kong Polytechnic University, Hung Hom, Kowloon, Hong Kong 999077, P. R. China. E-mail: meng.ni@polyu.edu.hk

Feifei Dong

Feifei Dong obtained his PhD in chemical engineering from Nanjing Tech University in 2014. He then worked as a research assistant and post-doctoral fellow at The Hong Kong Polytechnic University from 2014 to 2017. He is currently an associate professor at Guangdong University of Technology. His main research interests include solid oxide fuel cells, electrocatalysis, and inorganic non-metallic new energy materials.

Meng Ni

Meng Ni is a chair professor and associate dean (Research) at the Faculty of Construction and Environment, The Hong Kong Polytechnic University. He received his PhD degree in mechanical engineering from the University of Hong Kong in 2007. He is a Humboldt Fellow and a Co-Editor-in-Chief for Energy Reviews (Elsevier), a Senior Editor for Sustainable Energy Technologies and Assessments (Elsevier) and e-Prime (Elsevier), and an Associate Editor for the International Journal of Green Energy (Taylor & Francis) and Canadian Journal of Chemical Engineering (Wiley). His research interests include fuel cells, rechargeable metal–air batteries, electrochemical water-splitting, and electrochemical systems for low-grade waste-heat utilization.

1. Introduction

In the sustainable energy era, the ever-increasing demand for electricity provides a strong motivation for the advancement of fuel cell technology. Notably, solid oxide fuel cells (SOFCs), featuring high energy efficiency, low noise, flexible fuel adaptability, and minimal pollutant emissions, stand as the most efficient and eco-friendly energy conversion device among all counterparts.[1–5] SOFCs are generally composed of three principal components: an anode, an electrolyte, and a cathode, with a typical schematic structure depicted in Fig. 1. Nevertheless, conventional SOFCs, operating at high temperatures (HT, 800–1000 °C), are plagued by a series of detrimental effects, such as accelerated materials degradation, high operating costs, and slow start-up and shut-down cycles, considerably hampering their applicability in various energy-related domains.[6–9] Addressing these issues necessitates a transition from HT to intermediate-to-low temperatures (ILT, <800 °C) operation. Unfortunately, this transition is beleaguered by a barrier in performance, lagging far behind the requirements for widespread practical implementation. A crucial factor responsible for this underperformance is the sluggish reaction kinetics, particularly at the cathode, where the decline in operating temperature leads to significantly higher polarization loss compared to other components.[10–12] To attain the desired electrochemical performance, substantial efforts are warranted to pursue highly active and durable cathode materials for ILT-SOFCs.[13–17]

Among various alternatives, perovskite oxides have emerged as prominent candidates for cathode materials in virtue of their remarkable oxygen reduction reaction (ORR) activity and excellent accessibility, including but not limited to ABO_3 single perovskites, $AA'B_2O_6$ or $A_2BB'O_6$ double perovskites, and $A_{n+1}B_nO_{3n+1}$ Ruddlesden–Popper (RP) perovskites (Fig. 2a).[18–20] Within these categories, ABO_3 perovskites have gained significant popularity in scientific research. In a perfect cubic symmetrical structure of ABO_3 perovskite oxides, the larger A-site cations including alkaline, alkaline-earth, or lanthanide cations are coordinated with 12 surrounding oxygen anions, while the smaller B-site cations involving transition metal elements form a BO_6 octahedron in the 6-fold oxygen-coordinated position. Fig. 2b shows a schematic representation of the site occupancy in perovskite structures. Typical parent perovskite oxides, such as $LaMnO_3$, $SrCoO_3$, and $BaFeO_3$, can be broadly classified into two main categories based on their conductive properties: pure electronic conductors and mixed ionic–electronic conductors (MIEC).[21–25] Note that the pure electronic conductors, such as the $La_{1-x}Sr_xMnO_{3-\delta}$ (LSM) cathode, perform insufficiently at ILT since the active sites are confined to the electrode/electrolyte/gas triple-phase boundary (TPB). MIEC cathodes with simultaneous electronic and ionic conduction, by contrast, can extend the active region to the entire cathode surface, resulting in a significant improvement in oxygen reaction kinetics.[26,27] It follows that MIEC perovskite materials can function efficiently as oxygen reduction electrocatalysts for ILT-SOFCs operating in pure air. However, further investigations reveal their limitations as cathodes in the contaminated atmosphere. Specifically, the injection of CO_2 into the gas compartment causes a significant reduction in the power output and operational lifespan of SOFCs as a consequence of contaminant poisoning at the cathode side.[28,29] To mitigate these issues, the development of CO_2-tolerant cathodes is of paramount importance for the successful implementation of ILT-SOFCs.

According to the theory of Lewis acids and bases, a significant interplay occurs between perovskite oxide and CO_2 during the reaction, in which the former serves as a base and the latter acts as an acid.[30] The inherent acidity of CO_2 renders perovskite oxides susceptible to CO_2 poisoning. As a result, the generated electrically insulated carbonates cover the active sites on the cathode surface, intercepting oxygen adsorption and diffusion, thereby giving rise to an irreversible degradation in performance. Numerous efforts are therefore ongoing to develop novel CO_2-resistant cathodes.[31–33] Encouragingly, entirely CO_2-resistant cathodes have been successfully constructed in the lab-scale test. Benefiting from the thermodynamically and kinetically stable nature against CO_2 poisoning, these cathodes can maintain a consistent level of electroactivity even in a CO_2-containing atmosphere for ILT-SOFCs.[34,35] Notwithstanding, research and development on such cathodes is still limited due to the absence of systematic methodologies. Considering the scarcity of completely CO_2-resistant cathodes, those with a slow degradation rate in impure air also need to be acknowledged, since they account for a substantial fraction of the overall CO_2-resistant cathode family in terms of existing reports.[9,26]

In view of the current shortage of well-rounded reports summarizing the recent progress in CO_2-resistant perovskite cathodes, this paper provides a thorough review of the latest research advances in this vital field. Specifically, this review primarily focuses on the following aspects. Firstly, the underlying mechanisms of CO_2-poisoning reactions are explored for a comprehensive understanding of the interaction between electrodes and contaminants. Afterwards, credible approaches for appraising the resistance to CO_2 are proposed, including

Zhan Lin

Zhan Lin obtained his PhD degree from North Carolina State University in 2010. After that, he worked as a postdoctoral research associate at Oak Ridge National Laboratory and University of California, Berkeley from 2011 to 2013. He was appointed as a full professor at Zhejiang University in 2014. Currently, he is a full professor and research leader in the School of Chemical Engineering and Light Industry at Guangdong University of Technology. His research mainly focuses on advanced materials for energy storage and conversion.

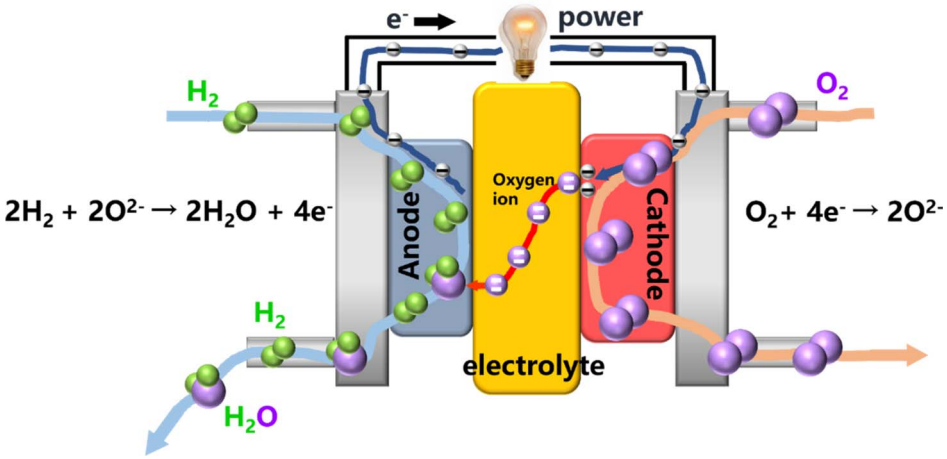

Fig. 1 Schematic representation of the operational principle of SOFCs.

acidity, average metal–oxygen bond energy, deterioration rate, *etc.* Corresponding strategies to enhance CO_2 tolerance are also detailed, with a selection of exemplary cases provided to illustrate the effectiveness of these methods. Moreover, typical characterization techniques are enumerated and discussed, placing particular emphasis on the role of *in situ* and *operando* characterizations that are central to the development of fundamental research. In the end, a brief summary and outlook on future challenges and perspectives in this burgeoning field are highlighted to provide a comprehensive blueprint toward an efficient and affordable future for CO_2-tolerant cathodes for ILT-SOFC technology.

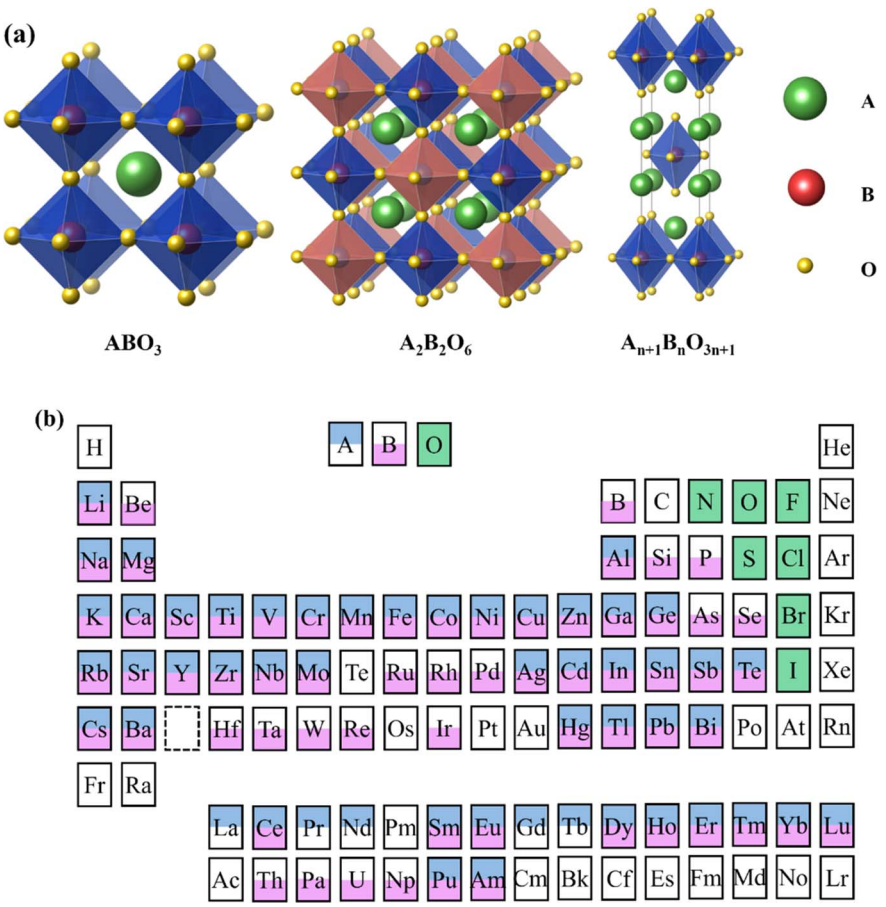

Fig. 2 (a) Schematic illustration of typical perovskite crystal structures. (b) Comprehensive element distribution chart based on site occupancy in perovskite structures.

2. Research progress on CO_2-tolerant perovskite cathodes

Perovskite compounds, owing to their intrinsic nature, are highly susceptible to CO_2 as well as other acidic gases, meaning that they suffer from severe corrosion. Such vulnerability can lead to irreversible structural transition and rapid performance deterioration, even when exposed to trace amounts of CO_2 in the air (~0.03 vol%), which is primarily attributed to the inherent alkalinity of their metallic constituents. In the ABO_3-type structure of perovskite oxides, the A-site metal cations generally possess higher basicity and larger ionic sizes compared to their B-site counterparts. As a result, in the presence of CO_2, these A-site metal cations are more prone to dissociation from the structural framework and react to form carbonates associated with A-site elements.[36] The overall reaction can be described as follows (eqn (1)):

$$ABO_3 + CO_2 \leftrightharpoons ACO_3 + BO_2 \quad (1)$$

In reality, the ORR chiefly proceeds through the diffusion of oxygen into porous cathodes and adsorption of oxygen onto cathode surfaces, resulting in oxygen reduction and ion migration. However, these processes are detrimentally affected by the presence of atmospheric CO_2.[37–40] As illustrated in Fig. 3, CO_2 molecules competitively occupy the active sites and readily form catalytically inert carbonates. These carbonates effectively block ambient oxygen from the electroactive regions, rendering a significant number of active sites non-functional, which, in turn, leads to undesirable reaction kinetics.[41,42] Additionally, the presence of CO_2 can induce irreversible structural changes in the perovskite oxide. The formation of carbonates can cause lattice distortion and phase transitions, further compromising the structural integrity and electrochemical performance of the perovskite cathode. To address this fatal drawback, a pivotal approach is to minimize the surface coverage of carbonate sediments through external interventions.

The detrimental effects of CO_2 poisoning could be modulated by various external conditions, including operating temperature, CO_2 partial pressure, exposure duration, *etc.*[43–49] Notably, carbonate species are inherently temperature-sensitive. They tend to decompose in the HT regime, but remain metastable under ILT conditions. Hence, to alleviate CO_2-induced degradation, operating at elevated temperatures is generally recommended. When considering gas concentration, a CO_2-rich environment is favorable for metal cation segregation and carbonation behavior, thereby accelerating the performance deterioration of oxygen electrocatalysts. For instance, Rehman *et al.* observed that the $SrFe_{0.8}Nb_{0.1}Ta_{0.1}O_{3-\delta}$ electrode exhibited a dramatic increase in polarization impedance from to 0.3 to 14.0 Ω cm^2 as the CO_2 partial pressure varied from 0 to 10 vol%. This degradation was attributed to exacerbated Sr segregation and carbonate deposition under highly CO_2-concentrated conditions, as verified by associated X-ray photoelectron spectroscopy (XPS) analysis.[50] Regarding exposure duration, it is a crucial factor often considered when assessing the degradation patterns of the investigated electrodes.

For the efficient and durable operation of SOFCs, there is an urgent need for versatile air electrode materials with complete CO_2-resistance. Encouragingly, significant breakthroughs at the laboratory scale have been achieved in recent years. Major research milestones are schematized in Fig. 4.[34,35,38,51–60] However, despite these commendable advancements, transitioning these catalysts to industrial-scale applications remains a challenge, which is primarily due to the high acquisition costs and limited availability of certain metal resources (*e.g.*, Co, Nb, and Ta), as well as complex fabrication processes.

Electrode reversibility between pure air and contaminated atmospheres, a crucial factor influencing operational lifespan, has also increasingly come under the spotlight.[55,61] Virtually, the catalytic activity of a poisoned electrode could recover upon the removal of gaseous contaminants, sometimes even reverting to its initial level given sufficient exposure time in pure air. Operating at elevated temperatures creates a conducive environment for enhanced oxygen activation and reduced CO_2 adsorption. As reported by Zhang *et al.*, the electroactivity of $Ba_{0.5}Sr_{0.5}Co_{0.8}Fe_{0.2}O_{3-\delta}$ (BSCF) returned to its original state only at 700 °C when alternated between CO_2-enriched and pure air atmospheres, whereas other cases operating below this temperature seldom attained full reversibility. A parallel trend was observed for the $SrSc_{0.175}Nb_{0.025}Co_{0.8}O_{3-\delta}$ (SSNC) cathode,[62] a phenomenon largely attributed to the sluggish oxygen reaction kinetics at reduced temperatures. Hence, perovskite oxides with inherently high susceptibility to CO_2 may lack full recoverability; in contrast, those demonstrating complete reversibility offer promising prospects as practical air electrodes at reduced temperatures. A compilation of recently reported perovskite-type electrodes with reversible responses is tabulated in Table 1.[63–71]

Element segregation also poses a significant challenge to the application of perovskite air electrodes, especially for those perovskite oxides where the A-site is occupied by alkaline earth elements with large ionic radii, such as Ba and Sr.[72–75] Plagued by the size mismatch between Ba^{2+}/Sr^{2+} and B-site cations, the overall elastic energy and lattice strain are inclined to rise, leading to the segregation of large-sized cations to the free surfaces or interfaces. Notably, these segregated specimens primarily manifest as metal oxides, and further transform into

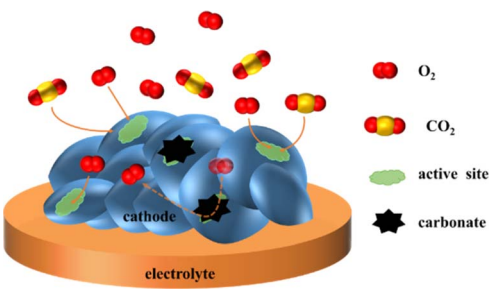

Fig. 3 Schematic illustration of the reaction between oxygen and carbon dioxide upon the surface.

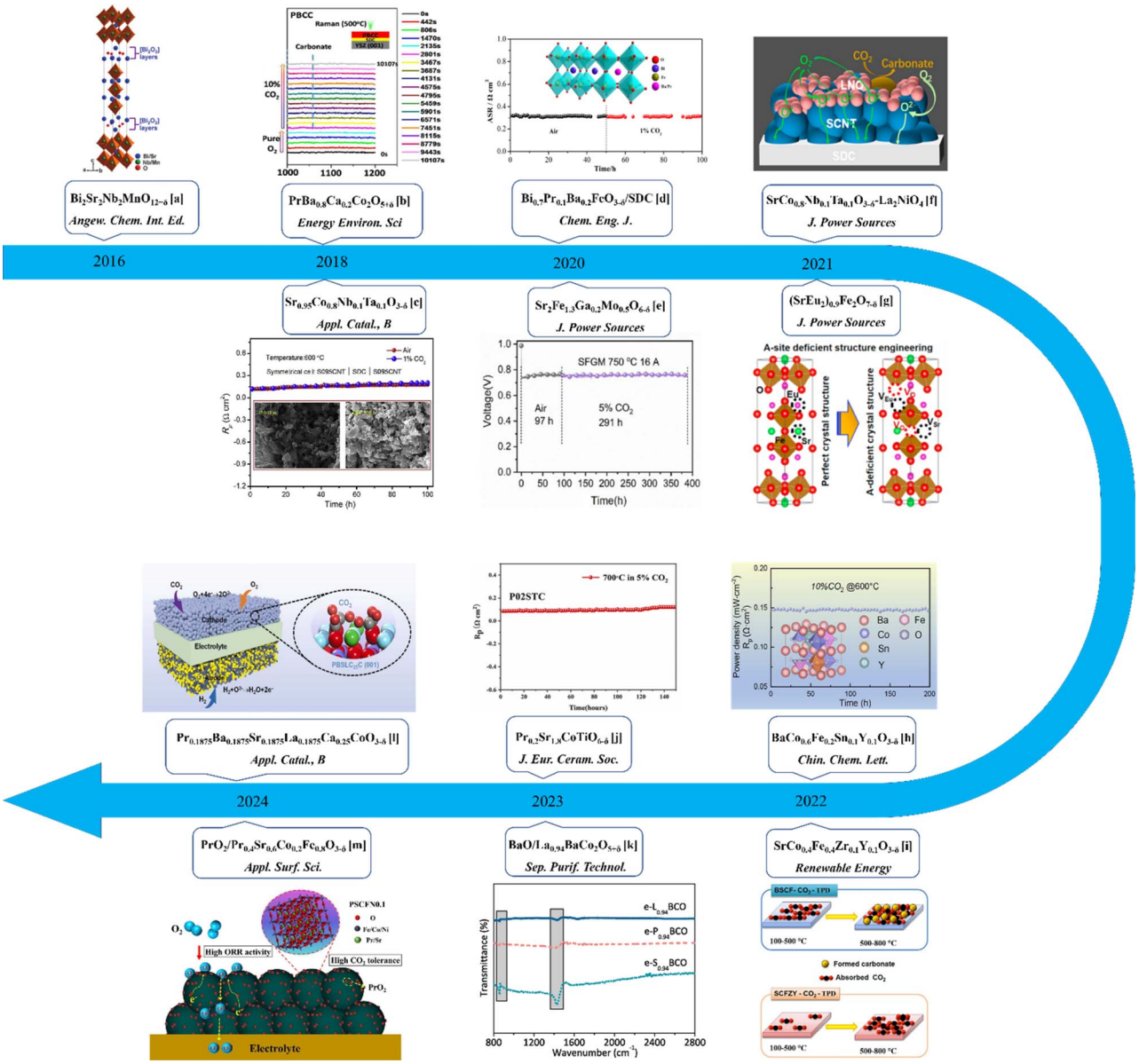

Fig. 4 Advancements in perovskite cathodes with complete CO_2-tolerance. (a) Reproduced with permission.[34] Copyright 2016, John Wiley and Son. (b) Reproduced with permission.[35] Copyright 2018, Royal Society of Chemistry. (c) Reproduced with permission.[38] Copyright 2018, Elsevier. (d) Reproduced with permission.[51] Copyright 2020, Elsevier. (e) Reproduced with permission.[52] Copyright 2020, Elsevier. (f) Reproduced with permission.[53] Copyright 2021, Elsevier. (g) Reproduced with permission.[54] Copyright 2021, Elsevier. (h) Reproduced with permission.[55] Copyright 2022, Elsevier. (i) Reproduced with permission.[56] Copyright 2022, Elsevier. (j) Reproduced with permission.[57] Copyright 2023, Elsevier. (k) Reproduced with permission.[58] Copyright 2023, Elsevier. (l) Reproduced with permission.[59] Copyright 2024, Elsevier. (m) Reproduced with permission.[60] Copyright 2024, Elsevier.

the bulk-phase-like carbonates upon exposure to CO_2. It is noteworthy that dopants with high valence states (*e.g.*, Nb^{5+}, Ta^{5+}, and Ti^{4+}) play a significant role in suppressing the segregation effect.[76–78] These thermodynamically stabilizing agents typically aid in reducing the lattice strain, strengthening the perovskite framework, and thus alleviating the segregation effect. Additionally, medium-entropy design can improve CO_2 resistance by reducing surface segregation due to the unique properties, such as lattice distortion and stress-field change.[79]

3. Evaluation methods for CO_2 tolerance in perovskite cathodes

To the best of our knowledge, the CO_2-tolerance level of perovskite-type electrodes can be determined through a variety of assessment methods, including acidity, average metal–oxygen bond energy (ABE), and deterioration rate, among others. In this section, we will systematically discuss and elucidate these determining factors.

Table 1 Relevant data regarding perovskite cathodes with reversible response

Cathode	Temperature/°C	Area-specific resistance (ASR)/Ω cm^2			Ref.
		Pure air	Air containing CO_2	CO_2 removal	
$Ba_{0.75}Sr_{0.25}Fe_{0.95}P_{0.05}O_{3-\delta}$	600	0.1	~0.75 (1 vol%)	0.1	63
$Ba_{0.95}Fe_{0.7}Co_{0.2}Sc_{0.1}O_{3-\delta}$		0.025	~1 (1 vol%)	0.025	64
$Sr_{0.95}Nb_{0.1}Co_{0.9}O_{3-\delta}$		0.056	~0.655 (10 vol%)	~0.056	65
$Ba_{0.5}Sr_{0.5}Co_{0.8}Fe_{0.2}O_{3-\delta}$–$Pr_2O_2SO_4$		0.055	0.505 (10 vol%)	0.061	66
$Ba_{0.9}Co_{0.7}Fe_{0.2}Nb_{0.1}O_{3-\delta}$	650	0.085	~0.205 (3 vol%)	0.085	67
$La_{0.8}Sr_{0.2}MnO_{3-\delta}$–$Ba_{0.5}Sr_{0.5}Co_{0.8}Fe_{0.2}O_{3-\delta}$		~0.58	0.819 (10 vol%)	0.58	68
$SrSc_{0.175}Nb_{0.025}Co_{0.8}O_{3-\delta}$	700	~0.02	~0.18 (10 vol%)	~0.02	62
$Ba_{0.95}La_{0.05}Fe_{0.85}Cu_{0.15}O_{3-\delta}$		0.091	~0.36 (10 vol%)	0.091	69
$BaFe_{0.95}Pr_{0.05}O_{3-\delta}$		0.097	~0.13 (20 vol%)	~0.097	70
$Bi_{0.5}Sr_{0.5}Fe_{0.85}Ti_{0.15}O_{3-\delta}$		0.085	0.108 (20 vol%)	0.086	71

3.1 Acidity

Metal oxides with higher acidity generally exhibit enhanced CO_2 resistance. From this perspective, the incorporation of high-acidity agents into the perovskite framework emerges as a promising strategy for boosting CO_2-tolerance. However, as a qualitative character, acidity poses challenges for quantification in practical assessment. Addressing this, Nak *et al.* proposed a scale for the acidity of 101 metal oxides in terms of the $N_M - 2\delta_M$ value, where N_M represents the formal oxidation state of the metal and δ_M stands for Sanderson's partial charges of the metal ion. This metric serves as a tool for sizing up the acidity, with a higher $N_M - 2\delta_M$ value indicative of increased acidity.[80] On the grounds of the compiled data (Table 2),[80] the acidity of metal ions at specific perovskite sites can be ranked in descending order as follows:

A-site:

$$Bi^{5+} > Y^{3+} > Dy^{3+} > Tb^{3+} > Gd^{3+} > Eu^{3+} > Sm^{3+} > Nd^{3+} > Ca^{2+} > Pr^{3+} > Ce^{3+} > Sr^{2+} > Ba^{2+} > La^{3+} > Ag^{+} > Li^{+} > Na^{+} > K^{+} > Rb^{+} > Cs^{+}$$

B-site:

$$Mn^{7+} > Cr^{6+} > Mo^{6+} > Bi^{5+} > W^{5+} > As^{5+} > V^{5+} > Sb^{5+} > Nb^{5+} > Co^{4+} > Ta^{5+} > Mn^{4+} > Ge^{4+} > Pb^{4+} > Sn^{4+} > Ti^{4+} > Co^{3+} > Zr^{4+} > Ga^{3+} > Tl^{3+} > Hf^{4+} > Fe^{3+} > In^{3+} > Al^{3+} > Sc^{3+} > Lu^{3+} > Yb^{3+} > Tm^{3+} > Zn^{2+} > Y^{3+} > Hg^{2+} > Er^{3+} > Ho^{3+} > Cu^{2+} > Cd^{2+} > Co^{2+} > Ni^{2+} > Fe^{2+} > Mg^{2+} > Ce^{3+}$$

Table 2 Increasing order of the $N_M - 2\delta_M$ value for metal oxides

M_xO_y	$N_M - 2\delta_M$	M_xO_y	$N_M - 2\delta_M$	M_xO_y	$N_M - 2\delta_M$	M_xO_y	$N_M - 2\delta_M$	M_xO_y	$N_M - 2\delta_M$
Cs_2O	0.300	WO	0.984	Dy_2O_3	1.508	Cr_2O_3	2.250	GeO_2	3.614
Rb_2O	0.317	NbO	1.006	CoO	1.508	Al_2O_3	2.274	MnO_2	3.663
K_2O	0.347	Pr_2O_3	1.064	CdO	1.512	In_2O_3	2.467	Ta_2O_5	3.694
Na_2O	0.375	MoO	1.074	CuO	1.515	Mn_2O_3	2.493	CoO_2	3.804
Li_2O	0.402	CaO	1.099	Ho_2O_3	1.538	Fe_2O_3	2.493	NiO_2	3.866
Cd_2O	0.411	Nd_2O_3	1.139	Er_2O_3	1.582	HfO_2	2.503	Nb_2O_5	3.895
Ga_2O	0.447	Pm_2O_3	1.221	HgO	1.587	Tl_2O_3	2.513	W_2O_5	3.939
Tl_2O	0.478	CrO	1.233	Y_2O_3	1.591	Ga_2O_3	2.580	Mo_2O_5	4.107
Ag_2O	0.662	MgO	1.266	ZnO	1.596	ZrO_2	2.591	Bi_2O_5	4.450
HfO	0.697	Sm_2O_3	1.274	Ta_2O_3	1.627	TaO_2	2.627	Sb_2O_5	4.506
YO	0.770	Eu_2O_3	1.322	Tm_2O_3	1.634	Co_2O_3	2.634	V_2O_5	4.531
TaO	0.800	SnO	1.336	Yb_2O_3	1.670	Ni_2O_3	2.696	As_2O_5	4.670
La_2O_3	0.855	FeO	1.393	Lu_2O_3	1.698	WO_2	2.863	Cr_2O_5	4.676
ZrO	0.855	MnO	1.401	Zr_2O_3	1.712	NbO_2	2.877	Mn_2O_5	4.860
GeO	0.882	Gd_2O_3	1.402	W_2O_3	1.855	MoO_2	2.981	WO_5	5.007
ScO	0.931	Tb_2O_3	1.440	Sc_2O_3	1.883	TiO_2	3.046	Ni_2O_5	5.055
BaO	0.938	BeO	1.456	Nb_2O_3	1.883	VO_2	3.270	MoO_3	5.340
VO	0.961	PbO	1.494	Ti_2O_3	1.930	CrO_2	3.468	CrO_3	5.890
SrO	0.978	NiO	1.501	Mo_2O_3	1.968	PbO_2	3.468	MnO_3	6.062
Ce_2O_3	0.979	Hf_2O_3	1.502	V_2O_3	2.109	SnO_2	3.473	Mn_2O_7	7.258
TiO	0.984								

Thereafter, such a methodology has been recognized as a credible approach to visually evaluate the acidity of various metal oxides.

To date, various heteroatomic metallic dopants with high acidity, such as Sb, Bi, Ti, Ga, *etc.*, have been explored to enhance the CO_2-resistance of perovskite materials.[81–86] Taking the Sb dopant as an illustrative example, owing to the augmented acidity of Sb^{5+} compared to $Fe^{3+/2+}$, Sb-incorporating $Bi_{0.5}Sr_{0.5}FeO_{3-\delta}$ ($Bi_{0.5}Sr_{0.5}Fe_{0.9}Sb_{0.1}O_{3-\delta}$) demonstrated a substantially reduced degradation rate relative to its undoped counterpart under identical CO_2 concentrations.[81] Xia *et al.* further proposed that the Sb-doped behavior is favorable for structural robustness and CO_2 adsorption/desorption capacity, hence resulting in superior CO_2-tolerance, as corroborated by the combined experimental and computational analyses.[82] To achieve better performance, a co-substitution strategy involving elements with strong acidity has been applied to the parent oxides. Representative examples include SSNC, $SrSc_{0.075}Ta_{0.025}Fe_{0.9}O_{3-\delta}$, $Nd_{0.2}Sr_{0.8}Nb_{0.1}Co_{0.9}O_{3-\delta}$, *etc.*, all of which have demonstrated increased resistance to CO_2 poisoning.[62,85–91] The above investigations underscore the promising potential of multi-cation synergy in developing highly CO_2-resistant cathode candidates.

3.2 Average metal–oxygen bond energy

The average metal–oxygen bond energy (ABE) has been identified as a critical metric for quantitatively assessing the CO_2-resistance.[92–94] A more negative ABE value signifies a stronger metal–oxygen interaction, which, in turn, implies a weaker CO_2 adsorption capacity. For perovskite oxides, the overall ABE value can be deduced from the sum of the average A–O and B–O bond energies. Taking $A'_xA''_{1-x}B'_yB''_{1-y}O_{3-\delta}$ as an illustration, the relevant equations are given as follows (eqn (2)–(6)):

$$\langle \mathrm{ABE} \rangle = \langle \mathrm{A{-}O} \rangle + \langle \mathrm{B{-}O} \rangle \quad (2)$$

$$\langle \mathrm{A{-}O} \rangle = \Delta\langle \mathrm{A'{-}O} \rangle + \Delta\langle \mathrm{A''{-}O} \rangle \quad (3)$$

$$\langle \mathrm{B{-}O} \rangle = \Delta\langle \mathrm{B'{-}O} \rangle + \Delta\langle \mathrm{B''{-}O} \rangle \quad (4)$$

$$\Delta\left\langle \mathrm{A'-O} \right\rangle = \frac{x_{\mathrm{A}}}{m \times \mathrm{CN_A}} \times \left(\Delta H_{\mathrm{A}_m\mathrm{O}_n} - m \times \Delta H_{\mathrm{A}} - \frac{n}{2} \times D_{\mathrm{O}_2}\right) \quad (5)$$

$$\Delta\left\langle \mathrm{B'-O} \right\rangle = \frac{x_{\mathrm{B}}}{m \times \mathrm{CN_B}} \times \left(\Delta H_{\mathrm{B}_m\mathrm{O}_n} - m \times \Delta H_{\mathrm{B}} - \frac{n}{2} \times D_{\mathrm{O}_2}\right) \quad (6)$$

where x_A and y_B denote the molar fractions of A- and B-site cations, respectively. $CN_{A(B)}$ signifies the coordination number of A- or B-site cations (with $CN_A = 12$ and $CN_B = 6$). $\Delta H_{A_mO_n(B_mO_n)}$ and $\Delta H_{A(B)}$ represent the enthalpy of formation for one mole of A_mO_n or B_mO_n and the sublimation energy of A- or B-site metal at a certain temperature, respectively. D_{O_2} is the dissociation energy of O_2 (~500.2 kJ mol^{-1}). The data required for these calculations can be sourced from the HSC chemistry software.

As such, the CO_2-tolerance of various samples can be estimated and compared based on their respective ABE values.

For instance, the calculated ABE values for $La_{0.6}Sr_{0.4}Co_{0.2}Fe_{0.8}O_{3-\delta}$ (LSCF) and BSCF are −316 kJ mol^{-1} and −274 kJ mol^{-1}, respectively, implying that the former possesses superior CO_2-resistance relative to the latter. This notion is corroborated by experiments conducted by Zhu *et al.*: the LSCF electrode displays a moderate relative increase in ASR values (~1.7-fold growth), while its counterpart BSCF experiences a more pronounced rise (~2.7-fold increase) under the same CO_2 atmosphere for 15 minutes.[34] In respect to the $Bi_{0.5}Sr_{0.5}FeO_{3-\delta}$ (BSF) electrode, Mo- or Ta-doping appears to enhance CO_2-resistance, as evidenced by the more negative ABE values after substitution.[95,96] Table 3 exhibits the ABE values of a range of perovskite cathodes,[34,38,62,85,88,95–99] among which the $Bi_2Sr_2Nb_2MnO_{12-\delta}$ (BSMN) oxide has the most negative ABE value, highlighting its exceptional capacity against contaminant poisoning amongst the listed candidates.

3.3 Deterioration rate

As another key quantitative parameter, the deterioration rate sheds light on the contaminant-resisting ability of the electrode over the span of exposure time. Ideally, a deterioration rate closer to zero denotes increased CO_2-resistance. Regrettably, a substantial number of perovskite materials display an undesirable degradation in a CO_2-containing environment. As an illustrative example, the $BaCo_{0.4}Fe_{0.4}Zr_{0.1}Y_{0.1}O_{3-\delta}$ (BCFZY) cathode, when exposed to 10 vol% CO_2-containing air at 700 °C, experiences a rise in polarization resistance from 0.503 to 0.682 Ω cm^2 over a 120 hour period.[76] Similarly, the classic $PrBaCo_2O_{5+\delta}$ (PBC) electrode experiences a steep increase in ASR value by 60% during a 30 hour operation in air with 5 vol% CO_2 at

Table 3 ABE values of various perovskite cathodes

Cathode	ABE/kJ mol^{-1}	Ref.	Cathode	ABE/kJ mol^{-1}	Ref.
$Ba_{0.5}Sr_{0.5}Co_{0.8}Fe_{0.2}O_{3-\delta}$	−274	34	$Nd_{0.2}Sr_{0.8}Nb_{0.1}Co_{0.9}O_{3-\delta}$	−290	88
$La_{0.6}Sr_{0.4}Co_{0.2}Fe_{0.8}O_{3-\delta}$	−316	34	$Bi_{0.5}Sr_{0.5}FeO_{3-\delta}$	−276.67	95
$Bi_2Sr_2Nb_2MnO_{12-\delta}$	−414	34	$Bi_{0.5}Sr_{0.5}Fe_{0.9}Ta_{0.1}O_{3-\delta}$	−296.97	95
$SrCo_{0.8}Nb_{0.1}Ta_{0.1}O_{3-\delta}$	−303.4	38	$Bi_{0.5}Sr_{0.5}Fe_{0.95}Mo_{0.05}O_{3-\delta}$	−284.59	96
$SrSc_{0.175}Nb_{0.025}Co_{0.8}O_{3-\delta}$	−293	62	$SrNb_{0.1}Fe_{0.9}O_{3-\delta}$	−302	97
$SrSc_{0.1}Fe_{0.9}O_{3-\delta}$	−292	85	$SrNb_{0.1}Co_{0.7}Fe_{0.2}O_{3-\delta}$	−294	97
$SrTa_{0.1}Fe_{0.9}O_{3-\delta}$	−304	85	$SrFe_{0.9}Hf_{0.1}O_{3-\delta}$	−302	98
$SrSc_{0.075}Ta_{0.025}Fe_{0.9}O_{3-\delta}$	−295	85	$Pr_{0.94}Ba_{0.7}Ca_{0.3}Co_2O_{5+\delta}$	−319	99

Table 4 The calculated deterioration rates of perovskite cathodes

Cathode	Operating conditions	Deterioration rate/Ω cm^2 min^{-1}	Ref.
$BaCo_{0.4}Fe_{0.4}Zr_{0.1}Y_{0.1}O_{3-\delta}$	1 vol% CO_2, 700 °C	$\sim 2.9 \times 10^{-5}$	76
$Ba_{0.95}Ca_{0.05}Co_{0.4}Fe_{0.4}Zr_{0.1}Y_{0.1}O_{3-\delta}$		$\sim 9.2 \times 10^{-6}$	76
$PrBa_{0.94}Co_{1.96}Ta_{0.04}O_{5+\delta}$		$\sim 4.4 \times 10^{-5}$	99
$Ba_{0.5}Sr_{0.5}Co_{0.8}Fe_{0.2}O_{3-\delta}$		$\sim 4.7 \times 10^{-5}$	101
$(Ba_{0.5}Sr_{0.5})(Co_{0.8}Fe_{0.2})_{0.9}Y_{0.1}O_{3-\delta}$		$\sim 4.0 \times 10^{-5}$	101
$Ba_{0.9}Co_{0.7}Fe_{0.3}O_{3-\delta}$		$\sim 1.6 \times 10^{-4}$	102
$Ba_{0.9}Co_{0.7}Fe_{0.3}O_{3-\delta}$ + 15 wt% Pr_6O_{11}		$\sim 2.4 \times 10^{-5}$	102
$BaFe_{0.95}Pr_{0.05}O_{3-\delta}$	10 vol% CO_2, 700 °C	$\sim 1.3 \times 10^{-5}$	70
$BaCo_{0.4}Fe_{0.4}Zr_{0.1}Y_{0.1}O_{3-\delta}$		$\sim 2.5 \times 10^{-5}$	76
$Ba_{0.95}Ca_{0.05}Co_{0.4}Fe_{0.4}Zr_{0.1}Y_{0.1}O_{3-\delta}$		$\sim 8.9 \times 10^{-6}$	76
$Pr_{0.94}BaCo_2O_{5+\delta}$		$\sim 2.5 \times 10^{-4}$	99
$Pr_{0.94}Ba_{0.7}Ca_{0.3}Co_2O_{5+\delta}$		$\sim 2.7 \times 10^{-5}$	99
$Ba_{0.6}La_{0.4}FeO_{3-\delta}$		$\sim 7.1 \times 10^{-4}$	103
$Ba_{0.6}La_{0.4}FeO_{3-\delta}$–$Ce_{0.8}Sm_{0.2}O_{2-\delta}$		$\sim 3.2 \times 10^{-4}$	103
$Ba_{0.5}Sr_{0.5}Co_{0.8}Fe_{0.2}O_{3-\delta}$		$\sim 4.5 \times 10^{-2}$	56
$SrCo_{0.4}Fe_{0.4}Zr_{0.1}Y_{0.1}O_{3-\delta}$		$\sim 1.1 \times 10^{-2}$	56
$Bi_{0.5}Sr_{0.5}FeO_{3-\delta}$		$\sim 3.7 \times 10^{-4}$	104
$Bi_{0.5}Sr_{0.5}Fe_{0.95}V_{0.05}O_{3-\delta}$		$\sim 1.4 \times 10^{-4}$	104
$Bi_{0.5}Sr_{0.5}Fe_{0.9}Zr_{0.1}O_{3-\delta}$		$\sim 2.2 \times 10^{-4}$	105
$PrBa_{0.5}Sr_{0.5}Co_{1.5}Fe_{0.5}O_{5+\delta}$		$\sim 9.4 \times 10^{-4}$	106
$La_2NiO_{4+\delta}$–$PrBa_{0.5}Sr_{0.5}Co_{1.5}Fe_{0.5}O_{5+\delta}$		$\sim 3.0 \times 10^{-4}$	106
$PrBa_{0.94}Co_2O_{5+\delta}$		$\sim 6.6 \times 10^{-5}$	107
$PrBa_{0.94}Co_{1.96}Ta_{0.04}O_{5+\delta}$		$\sim 3.8 \times 10^{-5}$	108
$SrCo_{0.7}Nb_{0.1}Ni_{0.2}O_{3-\delta}$		$\sim 5.6 \times 10^{-3}$	109
$Pr_{0.93}BaFe_2O_{5+\delta}$		$\sim 1.5 \times 10^{-4}$	110
$Bi_{0.5}Si_{0.5}Fe_{0.9}Sb_{0.1}O_{3-\delta}$	10 vol% CO_2, 650 °C	$\sim 3.3 \times 10^{-4}$	81
$SrSc_{0.025}Nb_{0.075}Fe_{0.9}O_{3-\delta}$		$\sim 1.3 \times 10^{-3}$	87
$SrCo_{0.85}Ta_{0.15}O_{3-\delta}$ + 4.2% SDC		$\sim 6.2 \times 10^{-4}$	111
$SrFe_{0.9}Ti_{0.1}O_{3-\delta}$		$\sim 3.3 \times 10^{-2}$	112
$SrFe_{0.8}Nb_{0.1}Ta_{0.1}O_{3-\delta}$	10 vol% CO_2, 600 °C	$\sim 2.3 \times 10^{-2}$	50
$Sr_{0.95}Li_{0.05}Fe_{0.8}Nb_{0.1}Ta_{0.1}O_{3-\delta}$		$\sim 1.9 \times 10^{-3}$	50
$SrCo_{0.8125}Sb_{0.1875}O_{3-\delta}$		$\sim 1.3 \times 10^{-3}$	82
$SrSc_{0.075}Ta_{0.025}Fe_{0.9}O_{3-\delta}$		$\sim 4.3 \times 10^{-2}$	85
$Ba_{0.5}Sr_{0.5}Co_{0.8}Fe_{0.2}O_{3-\delta}$		$\sim 2.3 \times 10^{-1}$	85
$SrNb_{0.1}Co_{0.7}Fe_{0.2}O_{3-\delta}$		$\sim 3.1 \times 10^{-3}$	97
$SrCo_{0.85}Ta_{0.15}O_{3-\delta}$ + 4.2% SDC		$\sim 1.6 \times 10^{-3}$	111
$Sr_{0.95}Ag_{0.05}Nb_{0.1}Co_{0.9}O_{3-\delta}$		$\sim 7.2 \times 10^{-3}$	113
$Sr_{0.95}Nb_{0.1}Co_{0.9}O_{3-\delta}$		$\sim 1.3 \times 10^{-2}$	113
$Ba_{0.5}Sr_{0.5}Co_{0.7}Fe_{0.2}Ni_{0.1}O_{3-\delta}$		$\sim 5.7 \times 10^{-2}$	114
$SmBaCo_2O_{5+\delta}$		$\sim 1.9 \times 10^{-2}$	115
$Sm_{0.8}Ca_{0.2}BaCo_2O_{5+\delta}$		$\sim 4.2 \times 10^{-3}$	115
$Ba_{0.75}Sr_{0.25}Fe_{0.95}P_{0.05}O_{3-\delta}$	1 vol% CO_2, 600 °C	$\sim 3.6 \times 10^{-4}$	63
$Ba_{0.95}Fe_{0.7}Co_{0.2}Sc_{0.1}O_{3-\delta}$		$\sim 2.0 \times 10^{-4}$	64
$SrNb_{0.1}Co_{0.7}Fe_{0.2}O_{3-\delta}$		$\sim 5.0 \times 10^{-3}$	97
$SrNb_{0.1}Fe_{0.9}O_{3-\delta}$		$\sim 2.7 \times 10^{-2}$	97
$SrNb_{0.1}Co_{0.9}O_{3-\delta}$		$\sim 1.2 \times 10^{-2}$	97
$SrFe_{0.9}Hf_{0.1}O_{3-\delta}$		$\sim 2.7 \times 10^{-3}$	98
$(La_{0.6}Sr_{0.4})_{0.95}Co_{0.2}Fe_{0.8}O_{3-\delta}$		$\sim 1.1 \times 10^{-3}$	116
$(La_{0.6}Sr_{0.4})_{0.95}Co_{0.2}Fe_{0.8}O_{3-\delta}$ + $Pr_{0.8}Ce_{0.2}O_{2-\delta}$		$\sim 1.1 \times 10^{-4}$	116
$PrLa_{0.4}Ba_{0.6}Fe_{0.8}Zn_{0.2}O_{5+\delta}$		$\sim 4.5 \times 10^{-6}$	117

800 °C.[100] Note that it is irrational to directly compare the increment of ASR values for evaluating the CO_2-tolerance of electrodes without considering the exposure time, yet to date, a unified criterion is lacking for ascertaining the level of deterioration rate. In light of this, this section embarks on a comparative study of the deterioration rate across 50 samples under various operating conditions for establishing a benchmark toward the CO_2-resistance of perovskite compounds, thus potentially providing a constructive guideline for the development of practical SOFC electrodes. The relevant information is summarized in Table 4, wherein the average deterioration rate of different samples is deduced in terms of reported results.

Remarkably, our findings suggest that the deterioration rate is predominantly dominated by two critical factors: operating temperatures and CO_2 concentrations. Based on the data available, it is inferred that a reduced deterioration rate can be attained by either elevating the operating temperature or

utilizing gas mixtures with lower CO_2 concentration. Under these investigated operating conditions, almost all samples demonstrate a less-than-optimal deterioration rate falling within the range of 10^{-5} to 10^{-2} Ω cm^2 min^{-1}. Notable exceptions are the $Ba_{0.95}Ca_{0.05}Co_{0.4}Fe_{0.4}Zr_{0.1}Y_{0.1}O_{3-\delta}$ (BCCFZY) and $PrLa_{0.4}Ba_{0.6}Fe_{0.8}Zn_{0.2}O_{5+\delta}$ (PLBFZ) cathodes, both of which showcase an ultralow deterioration rate below 1.0×10^{-5} Ω cm^2 min^{-1}. As a result, we posit that perovskite cathodes with such an impressively low level, comparable to completely CO_2-tolerant counterparts, may be acceptable for practical applications when operated within the temperature region of 600–700 °C, which deserve more attention in future exploration.

3.4 Other evaluation methods

3.4.1 CO_2 adsorption energy ($E_{ads(CO_2)}$). The CO_2 adsorption energy is derived using density functional theory (DFT) calculations, which is defined by the following equation:

$$E_{ads(CO_2)} = E_{CO_2/surface} - (E_{CO_2} + E_{surface}) \quad (7)$$

where $E_{CO_2/surface}$ denotes the total energy of the selected surface with adsorbed CO_2, E_{CO_2} is the energy of free CO_2, and $E_{surface}$ represents the total energy of the surface without CO_2 adsorption.[118,119] Generally, higher CO_2 adsorption energy implies weaker CO_2 adsorptive capacity and hence increased CO_2-resistance.

The BSCF electrode, renowned for its outstanding oxygen catalytic properties, unfortunately falls short in terms of CO_2-resistance, hence necessitating targeted modifications. In this regard, Lu *et al.* introduced a core–shell structured BSCF cathode integrated with an LSM oxide, which showcased improved durability in the CO_2 contaminated atmosphere. This enhancement is corroborated by first-principles study results, revealing a significant increase in the $E_{ads(CO_2)}$ from −0.158 to 0.414 eV for the A-site terminated surface and from −1.200 to 2.783 eV for the B-site terminated counterpart after the LSM coating.[120] As to the LSCF case, the computational analysis conducted by Chen *et al.* indicated that the surface modification with $BaCoO_{3-\delta}$ (BC) nanoparticles markedly weakened the CO_2 adsorption behavior, as evidenced by a shift in $E_{ads(CO_2)}$ values from −1.07 eV for the pristine LSCF to −0.54 eV for the composite configuration, thereby facilitating enhanced CO_2-resistance. Such hypothesis is highly consistent with experimental results, reinforcing its validity and credibility.[121] Hence, $E_{ads(CO_2)}$ is widely accepted as a vital indicator for assessing CO_2-tolerance capability.

3.4.2 Binding energy of lattice oxygen. The lattice oxygen binding energy, as derived from the O 1s orbitals using the XPS technique, has emerged as a reference terminology to gauge the basicity of perovskite compounds. In this case, higher binding energy denotes lower electron density (or equivalently, elevated oxidation state), and thus reduced basicity of perovskite cathodes, contributing to a better CO_2-resistance.[36] To illustrate, considering the $Sr(Co_{0.8}Fe_{0.2})_{1-x}Ti_xO_{3-\delta}$ derivatives, an increment in the Ti doping level from 0 to 0.4 prompts the lattice oxygen binding energy to rise from 528.4 to 529.1 eV. This variation leads to a stronger affinity between oxygen and metal ions, consequently mitigating the susceptibility to CO_2 intrusion.[122] Similarly, a Ta-substituted BSCF electrode demonstrated superior performance compared to its undoped counterpart in a CO_2-contaminated environment, a merit attributed to the higher lattice oxygen binding energy (529.13 eV as opposed to 528.72 eV).[123]

4. Strategies for developing CO_2-tolerant perovskite electrodes

In the pursuit of performance optimization of perovskite-type electrodes in the presence of atmospheric CO_2, researchers have put forward a series of feasible and effective strategies, involving doping, deficiency regulation, surface decoration, and multiphase mixing, all of which are delineated in this section.

4.1 Doping

Doping is widely recognized as a facile approach to tailor the intrinsic properties of perovskite oxides, such as crystal structure, thermal stability, and oxygen reduction kinetics. Until now, various methods including mono-doping, co-doping, and even multi-doping have been employed to enhance the resistance to contaminant poisoning.[124–126] For the sake of a clear discussion, these cases are categorized into three groups based on their primary elemental compositions, namely, cobalt-based, iron-based, and other perovskite compounds.

4.1.1 Cobalt-based perovskite oxides. Cobalt-based perovskite oxides have long been utilized as SOFC cathodes in virtue of their outstanding catalytic properties. $SrCoO_{3-\delta}$ (SC), a typical cobalt-based perovskite-type parent oxide, has undergone extensive investigation, especially as highly active air electrodes obtained by incorporating various agents. Zhu *et al.* illustrated that the CO_2 adsorption behavior of SC could be modulated *via* a co-doping strategy with Nb and Fe elements. Consequently, the $SrNb_{0.1}Co_{0.9-x}Fe_xO_{3-\delta}$ (SNCF*x*) derivatives exhibited augmented CO_2-resistance, correlating with increasingly negative ABE values with the increment of Fe concentration (Fig. 5a and b).[97] Through a tri-elemental doping strategy incorporating Fe, Zr, and Y, a newly developed $SrCo_{0.4}Fe_{0.4}Zr_{0.1}Y_{0.1}O_{3-\delta}$ (SCFZY) showed negligible sensitivity to CO_2. While operating in 1 vol% CO_2-containing air, the single cell with the SCFZY cathode demonstrated remarkable durability without apparent voltage degradation (Fig. 5c).[56] Furthering this line of research, Gao *et al.* designed a medium-entropy $SrCo_{0.5}Fe_{0.2}Ti_{0.1}Ta_{0.1}Nb_{0.1}O_{3-\delta}$ (SCFTTN) as a prospective air electrode for reversibility testing. The distribution of relaxation times (DRT) analysis depicted in Fig. 5d reveals the limited mass transport in the low-frequency process of the SCFTTN cathode upon encountering CO_2 contamination. However, this issue saw improvement after the removal of the contaminant, thereby conferring high reversibility to the SCFTTN electrode.[127] Other derivatives, including $SrCo_{0.85}Ta_{0.15}O_{3-\delta}$ (SCT15) and $SrCo_{0.9-x}Nb_{0.1}Ni_xO_{3-\delta}$, further substantiated the effectiveness of doping strategies in optimizing tolerance against CO_2 in the SC matrix.[111,128]

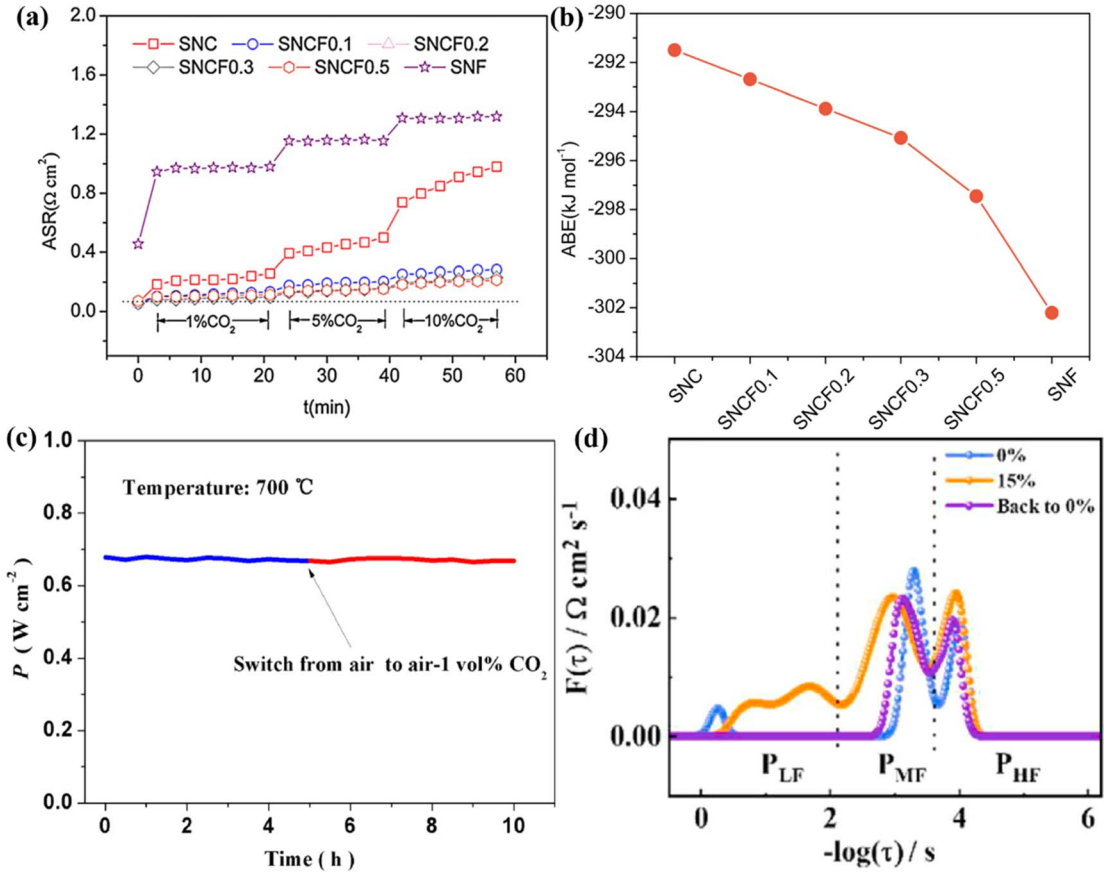

Fig. 5 (a) Time-dependent ASR of the SNCF*x* electrode at varying CO_2 concentrations and (b) ABE value of SNCF*x* electrodes. Reproduced with permission.[97] Copyright 2015, Elsevier. (c) Stability of the SCFZY cathode in the presence of 1 vol% CO_2. Reproduced with permission.[56] Copyright 2022, Elsevier. (d) DRT analysis results of the SCFTTN electrode in different atmospheres. Reproduced with permission.[127] Copyright 2022, Elsevier.

Regarding Ba-containing perovskite cobaltites, such as $BaCoO_{3-\delta}$ and double perovskite oxides $LnBaCo_2O_{5+\delta}$ (Ln = Pr, Sm, Gd), they are more susceptible to CO_2 poisoning due to the higher alkalinity of Ba^{2+}. To address this issue, reducing the Ba content and introducing dopants with a high valence state are usually attempted to suppress the carbonate formation.[129–131] As reported by Lu *et al.*, a $Ba_{0.9}Co_{0.7}Fe_{0.2}Zr_{0.1}O_{3-\delta}$ (B90CFZr)-derived single cell achieves a high peak power density (PPD) of 630 mW cm^{-2} at 700 °C in a 1 vol% CO_2-containing atmosphere, outperforming that of its pristine counterpart (559 mW cm^{-2}).[132] Supporting X-ray diffraction (XRD) and Fourier transform infrared (FT-IR) spectroscopy analyses well confirmed the excellent endurance of the B90CFZr sample after thermal treatment with CO_2. Benefiting from the multi-ion interaction effect, the novel $Ba_{0.9}La_{0.1}Co_{0.7}Fe_{0.2}Nb_{0.1}O_{3-\delta}$ electrode exhibited improved recovery ability when transitioning between CO_2 and air atmospheres.[130] Note that even trace amounts of foreign dopants have a significant impact on the resistance to CO_2 adsorption. Specifically, the incorporation of only 2 mol% Ta^{5+} enabled the $PrBa_{0.94}Co_{1.96}Ta_{0.04}O_{5+\delta}$ electrode to yield a low polarization resistance of 0.068 Ω cm^2 at 700 °C, maintaining a slight fluctuation even in a heavily CO_2 contaminated environment.[108] Furthermore, a 5 mol% Ca^{2+} substitution in the BCFZY cathode unveiled the polished surface without carbonate particles, in contrast to the undesired agglomeration observed for its undoped counterpart.[76]

4.1.2 Iron-based perovskite oxides. Iron-based perovskite oxides stand as widely investigated and cost-effective candidates for developing CO_2-tolerant cathodes, including $SrFeO_{3-\delta}$ (SF), $Bi_xSr_{1-x}FeO_{3-\delta}$, $PrBaFe_2O_{5+\delta}$, and so on.[133–139] Yu *et al.* demonstrated that the incorporation of U cations contributes to enhancing the structural stability of the SF oxide. As indicated by the XRD patterns in Fig. 6a and b, the U-doped SF sample exhibits admirable chemical stability after CO_2 treatment, a characteristic not mirrored by its unmodified counterpart.[133] Similarly, the co-substitution of redox-inactive Sc and Nb cations led to the $SrSc_{0.025}Nb_{0.075}Fe_{0.9}O_{3-\delta}$ (SSNF) electrode performing more stably up to 500 h in contaminated air.[87] Interestingly, an evident surface reconstruction was initiated by CO_2 removal in the SSNF compound. As shown in Fig. 6c, after removing contaminant gases, the SSNF electrode records an ASR value as low as 0.07 Ω cm^2 at 650 °C, only half of the original value (0.13 Ω cm^2) prior to CO_2 introduction. This substantial improvement is well ascribed to the manipulation

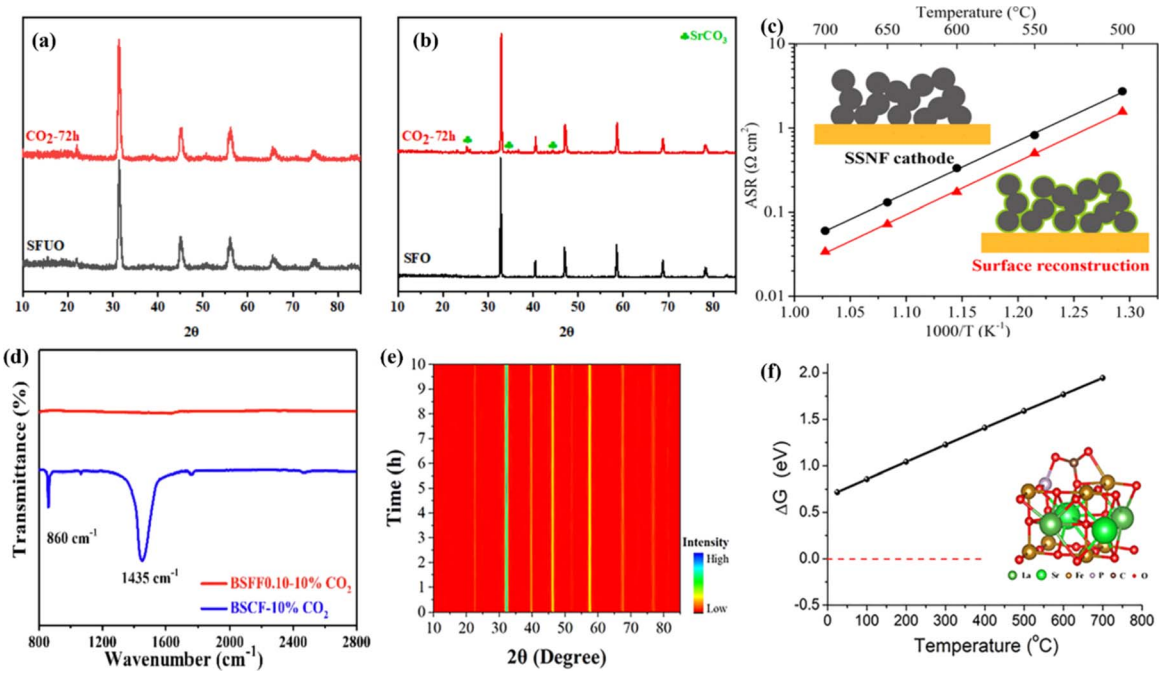

Fig. 6 XRD patterns for (a) U-doped SF and (b) undoped SF samples before and after CO_2 treatment. Reproduced with permission.[133] Copyright 2022, Elsevier. (c) An illustration of surface reconstruction in the SSNF cathode. Reproduced with permission.[87] Copyright 2020, American Chemical Society. (d) FT-IR spectra of BSCF and BSFF0.10 treated in 10% CO_2 at 600 °C. Reproduced with permission.[136] Copyright 2023, Elsevier. (e) Time course of XRD patterns for the LSFP powder measured at 700 °C in the CO_2-containing atmosphere and (f) the calculated Gibbs free energy for the reaction between LSFP and CO_2 with temperature. Reproduced with permission.[137] Copyright 2022, John Wiley and Son.

of CO_2-induced surface activation between the electrode and CO_2 molecules.

Emerging prominently, BSF-based perovskite compounds have gained recognition as potentially the most promising candidates for CO_2 resistance, largely owing to the highest acidity of Bi^{5+} compared to other A-site cations.[81] By combining with other dopants with both strong acidity and robust metal–oxygen bonds, these as-developed BSF-based electrodes are capable of conveying outstanding electroactivity under high CO_2 concentrations. Furthermore, optimal performance can be anticipated by the adjustment of dopant concentrations. Prominent examples in this category include $Bi_{0.5}Si_{0.5}Fe_{0.95}V_{0.05}O_{3-\delta}$, $Bi_{0.5}Si_{0.5}Fe_{0.95}Mo_{0.05}O_{3-\delta}$, and $Bi_{0.5}Si_{0.5}Fe_{0.95}Ta_{0.1}O_{3-\delta}$,[95,96,104] manifesting a bright future for BSF-based solutions in mitigating the challenges associated with CO_2 resistance.

Non-metal doping has also garnered significant attention for fostering resistance to contaminants. The recently reported $Bi_{0.7}Sr_{0.3}FeO_{2.9-\delta}F_{0.10}$ (BSFF0.10) electrode has exhibited superior CO_2 tolerance, standing in sharp contrast to the BSCF specimen, as evidenced by the absence of vibrational bands of CO_3^{2-} in the relevant FT-IR spectra (Fig. 6d).[136] Additionally, the P-incorporating $La_{0.5}Sr_{0.5}FeO_{3-\delta}$ (LSFP) compound was found to be thermodynamically stable against CO_2. *In situ* high-temperature XRD characterization unveils that the LSFP powder maintains its structural integrity without phase transition in CO_2-containing atmospheres. Complementing the empirical evidence, DFT calculations further underscore the thermodynamically durable nature (Fig. 6e and f).[137]

4.1.3 Other element-based alternatives. Apart from the prevailing perovskite cobaltites and ferrites, other element-based analogues have also demonstrated great anti-CO_2-poisoning ability.[140–146] For the nickel-based compounds, the $Nd_{1.8}La_{0.2}Ni_{0.74}Cu_{0.21}Ga_{0.05}O_{4+\delta}$ (NLNCG) oxide has been verified to be insensitive to CO_2. As displayed by the *I–V–P* curves in Fig. 7a, the anode-supported single cells with the PLNCG cathode perform efficiently without noticeable voltage decay in varying CO_2 gas mixtures, highlighting its feasibility for practical utilization.[140] Furthermore, a complex copper-based derivative originating from $Pr(Pr_{0.5}Ba_{1.5})Cu_3O_{7-\delta}$ has exhibited remarkable stability during long-term CO_2 exposure tests, suggesting its favorable functionality in impure air.[142] In respect to manganese-derived perovskite oxides, compounds such as $La_{0.5}Sr_{0.5}Mn_{0.875}Sc_{0.125}O_{3-\delta}$ and $Pr_{0.25}Nd_{0.25}Sr_{0.5}MnO_{3-\delta}$ are highly recommended for CO_2-resistant cathodes on account of their high endurance against gaseous contaminants.[143,146] Notably, BSMN stood as the first reported cathode with complete CO_2-tolerance in the current research.[34] As shown in Fig. 7b, when subjected to a short-term run under CO_2 exposure, the BSNM electrode delivers constant electroactivity with superior CO_2-tolerance, positioning it as a preferable option for the commercialization of SOFC cathodes.

4.2 Deficiency regulation

In comparison with cation-stoichiometric perovskites, non-stoichiometric counterparts generally demonstrate superior ORR activity, especially those with A-site deficiency. Such enhanced activity stems from the compensation effect

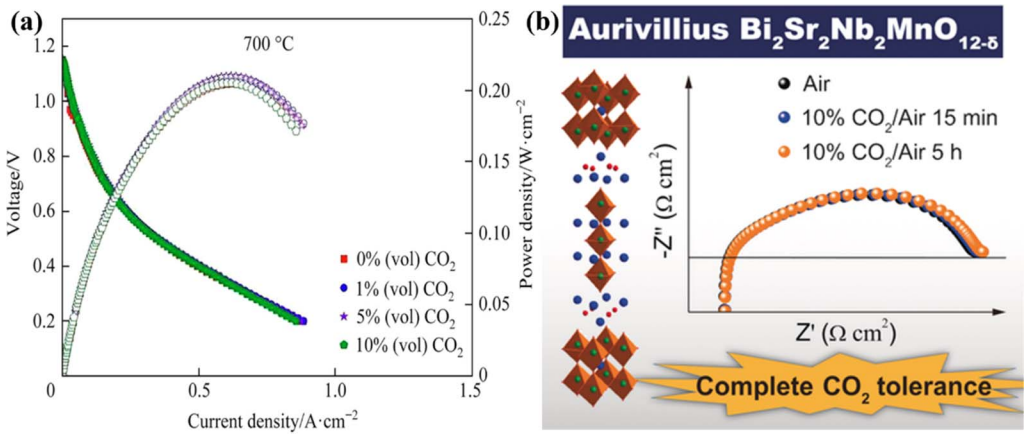

Fig. 7 (a) *I–V–P* curves of anode-supported single cells with the NLNCG cathode under different amounts of CO_2. Reproduced with permission.[140] Copyright 2023, Elsevier. (b) ASR value of BSNM in air and in air containing 10 vol% CO_2 with time. Reproduced with permission.[34] Copyright 2016, John Wiley and Son.

associated with cation deficiency, which is manifested as favorable properties such as high oxygen mobility and fast oxygen diffusion. These properties, in turn, play a significant role in mitigating CO_2 adsorption.[30] As an illustration, the Nyquist plots in Fig. 8a reveal that, under CO_2 exposure, the $Sr_{0.9}Ti_{0.3}Fe_{0.7}O_{3-\delta}$ (A-STF) electrode experiences a slower polarization resistance growth compared to the pristine STF within the same testing period (an increment of 0.07 Ω cm^2 *versus* 0.22 Ω cm^2). This phenomenon can be ascribed to the enhanced oxygen surface exchange and diffusion processes, as corroborated by the Bode plot results in Fig. 8b.[147] Similarly, He *et al.* observed that the A-site deficient nature renders the $La_{0.5}Ca_{0.5}MnO_{3-\delta}$ oxide more thermodynamically stable against both CO_2 and H_2O.[148] As reported by Peng *et al.*, $(SrEu_2)_{0.9}Fe_2O_{7-\delta}$-based symmetrical cells showed prominent anti-CO_2 corrosion performance with stable ASR values (Fig. 8c).[54] Additionally, a study on the A-site-deficient perovskite-type oxide $Ba_{0.95}Fe_{0.7}Co_{0.2}Sc_{0.1}O_{3-\delta}$ (BFCS0.95) highlights its remarkable reversibility between pure air and air containing CO_2, demonstrating superior CO_2 tolerance.[64] The above examples strongly suggest that A-site deficiency is conducive to alleviating the detrimental effect by CO_2 poisoning, especially for those perovskite oxides containing alkaline earth cations.

A-site non-stoichiometry has also been reported to facilitate the exsolution of B-site cations. Indeed, common B-site elements (*e.g.*, Co, Fe, Ni, and Cu) are thermodynamically unstable with a negative Gibbs free energy (ΔG) at elevated temperatures, thereby promoting their segregation from the lattice of the BO_2 unit cell within a deficient perovskite system. These elements eventually emerge as metal nanoparticles or metal oxides, acting as core catalytic active sites for the ORR.[149] In the case of $(La_{0.7}Sr_{0.3})_{0.95}(Co_{0.2}Fe_{0.8})O_{3-\delta}$ shown in Fig. 8d, A-site deficient behavior together with impregnation of $PrO_{2-\delta}$/$Pr_{0.8}Ce_{0.2}O_{2-\delta}$ nanoparticles assists in the formation of active $Sr_xCo_yO_z$ species, making it more active to oxygen uptake and hence improving CO_2 resistance.[116]

In addition to A-site deficiency, B-site deficiency also plays a significant role in enhancing CO_2 tolerance. For an example of B-site deficient perovskite oxide $Ba_{0.95}La_{0.05}(Fe_{0.8}Zn_{0.2})_{0.95}O_{3-\delta}$ (BLFZ0.95),[150] the CO_2-temperature programmed desorption (CO_2-TPD) profiles show smaller desorption peaks for BLFZ0.95 compared to non-deficient BLFZ, suggesting better resistance to CO_2 corrosion. XRD analysis after treatment in air with 1 vol% CO_2 at 600 °C reveals that BLFZ0.95 shows no significant formation of barium carbonate, unlike BLFZ, further confirming its superior CO_2 resistance.

4.3 Surface decoration

Surface decoration is identified as a diversified and complex avenue to improve the functionality of perovskite materials. This approach entails the development of a protective barrier on the material surface, weakening the direct interaction between the core backbone and contaminants, accompanied by enhanced surface oxygen adsorption, thus significantly contributing to improved ORR performance. Such heterostructured composites are rationally fabricated by hydrogen reduction or wet-chemistry methods, wherein the primary framework is commonly modified with additives, such as metal/alloy nanoparticles (Ag, Ru/Fe, *etc.*), fluorite-structured oxides ($PrO_{2-\delta}$/$Pr_{0.8}Ce_{0.2}O_{2-\delta}$, $La_{0.4875}Ca_{0.0125}Ce_{0.5}O_{2-\delta}$, *etc.*), or other secondary perovskite-type compounds (La_2NiO_4, $La_{0.8}Sr_{0.2}MnO_{3-\delta}$, $PrSrCoMnO_{6-\delta}$, *etc.*).[151–157] These decorating agents generally require high oxygen permeability, favorable catalytic activity, and acceptable stability, enabling the desirable oxygen reduction kinetics on the cathode surface.

Achieving perovskite cathodes with high electroactivity and CO_2-resistance is still challenging at the low-temperature region. Fortunately, this obstacle could be overcome *via* surface modification techniques. Zhu *et al.* developed an exsolved $Sr_{0.95}Ag_{0.05}Nb_{0.1}Co_{0.9}O_{3-\delta}$ composite with Ag nanoparticles (e-SANC) using a traditional exsolution process as depicted in Fig. 9a. Benefiting from the strong metal–substrate interaction, the e-SANC catalyst shows apparent insusceptibility to varying CO_2 concentrations with a slight relative increase in ASR values at 600 °C. This performance markedly surpasses that

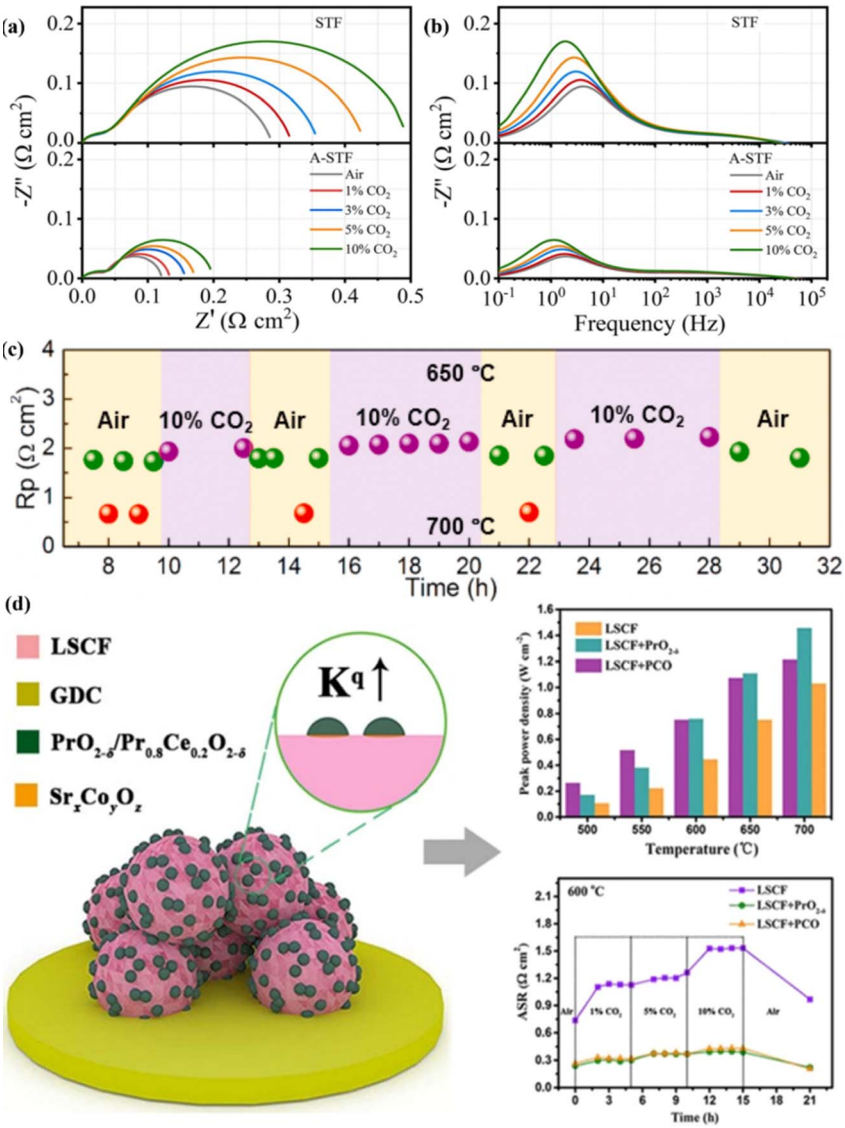

Fig. 8 Typical Nyquist (a) and Bode (b) plots of EIS data measured for symmetrical cells at varying CO_2 gas concentrations at 650 °C. Reproduced with permission.[147] Copyright 2022, Elsevier. (c) Thermal cycling of $(SrEu_2)_{0.9}Fe_2O_{7-\delta}$-based symmetrical cells. Reproduced with permission.[54] Copyright 2021, Elsevier. (d) Schematic diagram of microstructures of the LSCF-based composite electrode together with electrochemical performance assessment. Reproduced with permission.[116] Copyright 2020, American Chemical Society.

of the pristine SNC0.95 and benchmark BSCF (Fig. 9b), highlighting its substantial potential as a practical oxygen electrode at low temperatures.[113] Furthermore, surface decoration with La_2NiO_4 (LNO) particles endowed the $SrCo_{0.8}Nb_{0.1}Ta_{0.1}O_{3-\delta}$ (SCNT) electrode with acceptable performance degradation. As seen in Fig. 9c and d, a complete cell with the LNO-coated SCNT (SCNT-10LNO) cathode delivers extraordinarily higher PPDs of 279 and 256 mW cm^{-2} than those of the blank counterpart (179 and 140 mW cm^{-2}) in ambient air and 10% CO_2-containing air, respectively.[53] Interestingly, the introduction of a certain amount of metal carbonates has been reported to strengthen oxygen reduction performance. For instance, a 3% $SrCO_3$ coating on the LSCF cathode substantially improved the dynamic oxygen exchange capacity by nearly two orders of magnitude compared to the bare one.[158] In this sense, the strong coupling effect induced by the surface decoration method is highly favorable for ORR activity and CO_2-tolerance of SOFC cathodes.

The long-term effects of surface modifications on cathode performance are crucial for practical applications. A study on a novel heterostructured simple perovskite nanorod-decorated, A-site-deficient double perovskite $PrBa_{0.94}Co_2O_{5+\delta}$ (SPN-A-PBC) cathode, synthesized *via* an *in situ* exsolution process, illustrates this point.[107] The CO_2 durability measurements for the SPN-A-PBC electrode demonstrate excellent tolerance to CO_2, making it more viable for commercial applications.

Additionally, an infiltration method has also been shown to improve CO_2 tolerance in perovskite cathodes. For example, the infiltration of $Sm_{0.2}Ce_{0.8}O_{1.9}$ (SDC) into an SCT15 cathode is far less susceptible to degradation in the presence of 10% CO_2 compared to the pure SCT15 cathode.[111] Similarly, LNO coating on a $PrBa_{0.5}Sr_{0.5}Co_{1.5}Fe_{0.5}O_{5+\delta}$ (PBSCF) cathode using solution

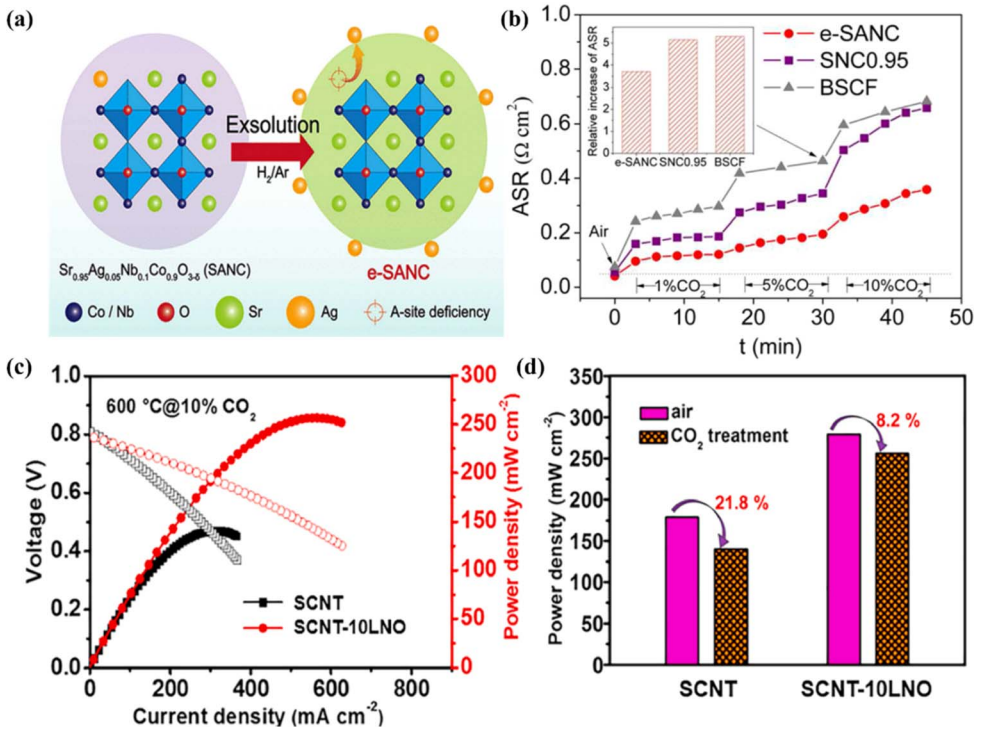

Fig. 9 (a) A schematic illustration of the exsolution process of the SANC specimen and (b) time-dependent ASR values of investigated cathodes as a function of CO_2 concentration in air. Reproduced with permission.[113] Copyright 2016, American Chemical Society. (c) *I–V–P* curves of single cells with SCNT and SCNT-10LNO cathodes treated in a 10% CO_2 atmosphere and (d) the corresponding power density comparison. Reproduced with permission.[53] Copyright 2021, Elsevier.

infiltration demonstrates recoverable performance degradation caused by CO_2 adsorption.[106] These examples highlight the effectiveness of the infiltration method in enhancing the CO_2 tolerance of SOFC cathodes.

4.4 Multiphase mixing

In contrast to the surface modification technique, the multiphase mixing method is regarded as a more straightforward and cost-effective strategy to produce hybrid composites with high molecular-level mixing uniformity, including ball-milling technology and one-pot synthesis. For the sake of high CO_2-resistance, such mixtures generally comprise a core cathode and a so-called "CO_2-tolerant aid", where the latter involves fluorite-based oxides (SDC, $Ce_{0.9}Gd_{0.1}O_{2-\delta}$ (GDC), *etc.*), or additional auxiliary perovskite materials. These additives are advantageous to not only extend the electroactive regions and thus improve the oxygen adsorption behavior, but also enhance the CO_2 resistance.[159–163] Illustratively, the CO_2 contamination test in Fig. 10a reveals that the SCNT-GDC electrode shows a diminished degradation rate of 0.0089 Ω cm^2 min^{-1}, which is an order of magnitude lower than that of the SCNT catalyst without GDC incorporation (0.013 Ω cm^2 min^{-1}). Further insights from the CO_2-TPD profiles in Fig. 10b identify a weaker desorption peak intensity for SCNT-GDC, signifying enhanced CO_2 resistance with the help of GDC.[159] Turning our attention to the $Bi_{0.7}Pr_{0.1}Ba_{0.2}FeO_{3-\delta}$ (BPBF) case, the incorporation of the SDC additive benefits the overall electrode resistance against CO_2. When assembled as symmetrical cells for a long-term run, the polarization impedance remains unchanged in the presence of gaseous contaminants (Fig. 10c), underlining its potential applicability in practical electrochemical devices.[51]

Noticeably, the various mixing ratios of material composition exert a pivotal impact on CO_2-tolerance. In the case of the $PrBaCo_2O_{6-\delta}$ (PBC)–$PrBaCoTaO_6$ (PBCT) composite cathode, the optimal CO_2-tolerance is acquired when the PBC content is augmented to up to 75 wt%.[162] Considering the absence of diffraction peaks corresponding to barium carbonates among all investigated samples (Fig. 10d), it is speculated that the addition of PBC, as opposed to PBCT, enables enhanced oxygen adsorption. Fig. 10e delineates the impedance and DRT spectra of the PBC–PBCT composite with a weight ratio of 75 : 25 before and after CO_2 treatment. Remarkably, the similarity between these two results manifests the highly kinetically active nature in an oxygen atmosphere despite the presence of CO_2. Accordingly, the exploration of the optimal ratio to achieve the best performance needs to move ahead for the development of CO_2-resistant composite cathodes.

5. Characterization

5.1 Conventional characterization

Conventional characterization tools for identifying carbonate species include XRD, FT-IR spectroscopy, Raman spectroscopy, transmission electron microscopy (TEM), CO_2-TPD, and so on.[164–170] The XRD technique is employed to detect the phase

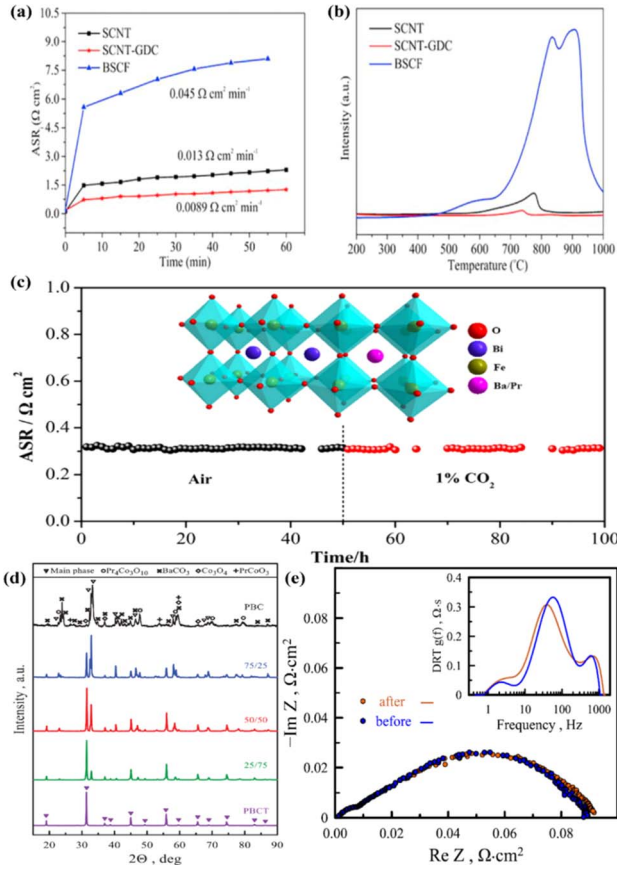

Fig. 10 (a) ASRs of the investigated electrodes as a function of time in 10 vol% CO_2 and (b) CO_2-temperature programmed desorption profiles of the investigated powders previously exposed to 10 vol% CO_2. Reproduced with permission.[159] Copyright 2018, Elsevier. (c) Durability of polarization ASR values of the BPBF electrode at 600 °C in air and 1 vol% CO_2. Reproduced with permission.[51] Copyright 2020, Elsevier. (d) XRD patterns of various electrode materials after treatment in 20 vol% CO_2 atmosphere and (e) impedance and DRT spectra of the PBC–PBCT composite with a weight ratio of 75 : 25 before and after CO_2 treatment. Reproduced with permission.[162] Copyright 2021, Elsevier.

structure of various carbonate groups. To be exact, the diverse carbonate structures are determined using the corresponding Joint Committee on Powder Diffraction Standards (JCPDS) cards, such as $BaCO_3$ (JCPDS card no. 11-0697 indexed to space group $Fm\bar{3}m$; JCPDS card no. 41-0373 assigned to space group *Pnma*), $SrCO_3$ (JCPDS card no. 05-0418), $Sr_{0.2}Ba_{0.8}CO_3$ (JCPDS card no. 47-0223), $Sr_{0.5}Ba_{0.5}CO_3$ (JCPDS card no. 47-0224), and $Sr_{0.8}Ba_{0.2}CO_3$ (JCPDS card no. 46-0746).[64,87] Regarding FT-IR and Raman spectroscopy characterizations, both techniques are used to identify the precipitated carbonates. As obtained from the FT-IR spectra of the BSCF sample subjected to a CO_2 atmosphere, the characteristic vibration bands emerging at ~1430 cm^{-1} and ~880 cm^{-1} correspond to the C–O stretching mode of carbonate deposits and in-plane bending mode of absorbed CO_2, respectively. Meanwhile, in the Raman spectra, the peak situated at ~1070 cm^{-1} is ascribed to the symmetric stretching of CO_3^{2-}.[171,172] Furthermore, high-resolution TEM (HR-TEM) is employed to examine the morphological evolution of carbonate species. As documented by Gu *et al.*, the SSNF electrode performed favorable catalytic activity in the presence of atmospheric CO_2 contamination.[87] By means of TEM characterization, an amorphous $SrCO_3$ nanofilm was clearly detectable on the outer surface of the SSNF sample after contamination, which is indicative of the formation of a protective layer against CO_2 poisoning.

As to the CO_2-TPD measurement, the peak area determined by on-line mass spectrometry can be utilized to evaluate the CO_2 surface desorption capacity. For example, the area ratio derived from the CO_2-TPD curves of SC and $Nd_{0.2}Sr_{0.8}Nb_{0.1}Co_{0.9}O_{3-\delta}$ samples, calculated to be 6.3 : 1.0, suggests the stronger anti-CO_2-poisoning ability of the latter.[99] Besides, CO_2 adsorption typically involves two temperature-dependent processes, namely, low-temperature (<600 °C) physical adsorption and high-temperature (>600 °C) chemical adsorption. A study conducted by Xia *et al.* indicated that as the Sb doping content increases from 0.0625 to 0.1875, the chemical adsorption temperature of the as-obtained specimen decreases from 636 to 598 °C. This trend signifies a weakened CO_2 chemical adsorption energy, which is desirable for ameliorating CO_2-resistance.[82] A similar phenomenon was observed in the SNCF cathodes, where a reduction in adsorption temperature from 584 to 469 °C is achieved with Fe substitution at Co sites increasing from 0 to 1, agreeing with the facilitated CO_2-tolerance of the modified SNCF cathodes.[97]

5.2 *In situ* and *operando* characterizations

Despite their high accessibility, conventional characterization methodologies are somewhat constrained due to the complexity of test environments and the uncertainty of reaction mechanisms. In response to the challenges, *in situ*/*operando* studies have been increasingly carried out to elucidate the structure–activity relationships.[173–177]

The *in situ* surface enhanced Raman spectroscopy (SERS) technique has been employed to provide detailed insights into the surface properties of cathode materials under dynamic operating conditions. Utilizing this approach, Chen *et al.* discovered that the $PrBa_{0.8}Ca_{0.2}Co_2O_{5+\delta}$ (PBCC) cathode is more robust and less sensitive to CO_2 relative to the classic LSCF counterpart, as evidenced by the consistent state without visible carbonate peaks for PBCC in a CO_2 atmosphere over time.[35] Moreover, the decomposition temperature of carbonate precipitates can be determined by *in situ* powder X-ray diffraction (PXRD) measurements.[173] It is well known that carbonates are prone to decomposition at elevated temperatures. Operating under such conditions could considerably mitigate the CO_2 poisoning effect, thereby paving the way for enhanced performance of SOFCs.

To shed light on the surface segregation phenomenon, Yu *et al.* utilized synchrotron-based total reflection X-ray fluorescence (TXRF) in conjunction with scanning transmission electron microscopy (STEM) techniques to determine the chemical composition of surface precipitates on the $La_{0.7}Sr_{0.3}Co_{0.2}Fe_{0.8}O_{3-\delta}$ (LSCF-7328) film sample.[175] Shown in Fig. 11a is the three-

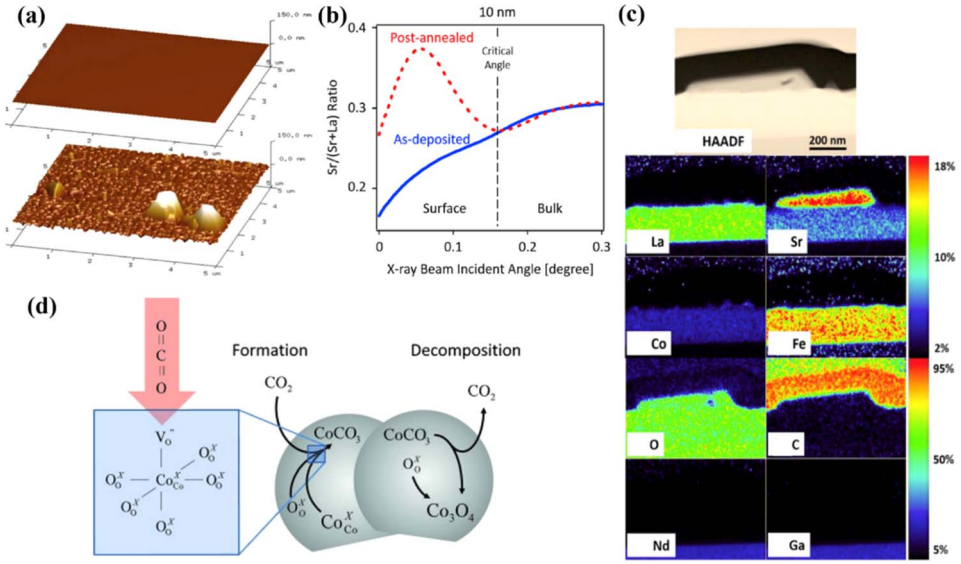

Fig. 11 (a) Three-dimensional AFM images of as-deposited and post-annealed LSCF-7328 sample surfaces; (b) processed TXRF data for LSCF-7328 before and after annealing; (c) a STEM high-angle annular dark-field (HAADF) image of the precipitate region of LSCF-7328. Reproduced with permission.[175] Copyright 2016, Elsevier. (d) Reaction mechanisms proposed between LSCF and CO_2. Reproduced with permission.[178] Copyright 2014, John Wiley and Son.

dimensional atomic force microscopy (AFM) images of the as-deposited and post-annealed LSCF-7328 samples. Clearly, after exposure to CO_2, the emergence of blocky deposits with various sizes on an uneven surface can be distinctly observed. These precipitates are identified as SrO bulk with a $SrCO_3$ capping layer, and the observed surface roughness is ascribed to cobalt enrichment, as verified by TXRF (Fig. 11b) and STEM results (Fig. 11c). This observation accounts for the diminished activity and stability of the LSCF-7328 cathode, highlighting the need for mitigation strategies.

Operando X-ray absorption spectroscopy (XAS), comprising X-ray absorption near edge structure and extended X-ray absorption fine structure analyses, serves as a powerful tool for probing the local atomistic and electronic structures of targeted elements. As reported by Lai *et al.*, the XAS results from the LSCF thin film indicated that atmospheric CO_2 is capable of inducing higher oxidation state of transition metal cations in conjunction with more oxygen ligands.[178] Synchrotron-based XPS was also adopted to further determine the chemical composition of the LSCF sample after contaminant treatment. By gaining insights from both XAS and XPS analyses, this study inferred that CO_2 preferentially interacts with Co to form cobalt carbonates, which subsequently decompose at elevated temperatures accompanied by the depletion of oxygen vacancies, consequently contributing to performance degradation of the LSCF electrode. The speculative reaction mechanism is schematically illustrated in Fig. 11d.

6. DFT calculations

DFT-based calculations are employed to gain an in-depth understanding of CO_2 adsorption behavior at the atomic level. The interaction capacity between perovskite oxides and CO_2 adsorbates can be reflected by specific quantifiable parameters, that is, CO_2 adsorption energy, surface energy, and Bader charge number.[179,180] Considering the different effects of CO_2 adsorption on various metal oxide terminations, these factors are generally determined in individual AO- and BO_2-terminated situations. For the $LaFeO_3$-based system, Su *et al.* illustrated that the BO_2-terminated surface is less susceptible to CO_2 in contrast to its AO-terminated counterpart in virtue of its higher surface energy.[138] Furthermore, this research demonstrated that compared to Sr substituents, Ca dopants are more favorable for making the FeO_2-terminated surface energetically stable in the presence of CO_2. This is substantiated by the observation of the larger CO_2 adsorption energy (−0.50 eV) for the Ca-doped samples than that of the Sr-incorporating ones (−1.04 eV), which is responsible for the improved CO_2 tolerance. Similar insights can also be accessible from Dai's work.[144] It is noteworthy that a high concentration of oxygen vacancies has a negative influence on CO_2 adsorption energy, giving rise to the generation of more carbonate sediments.[35,97] Such an issue warrants significant attention in the pursuit of developing CO_2-tolerant cathode materials.

Bader charge analysis elucidates the charge transfer processes between CO_2 adsorbates and metal oxide adsorbents, establishing a crucial link to intrinsic properties against CO_2. Huan *et al.* utilized this method to evaluate the chemical CO_2 adsorption ability of Al-doped and pristine $SrFeO_3$ oxides.[181] Their findings indicated that the Fe–O terminated (001) facet with the integration of Al is inclined to accept fewer electrons (−0.019 *versus* −0.191 e^-), implying that Al substitution engenders higher charge transfer resistance and thus less generation of carbonates. On a similar note, Li *et al.* illustrated the local charge-density fluctuations during the ORR process in the $SrCO_3$-modified LSCF model.[158] As depicted in Fig. 12, more

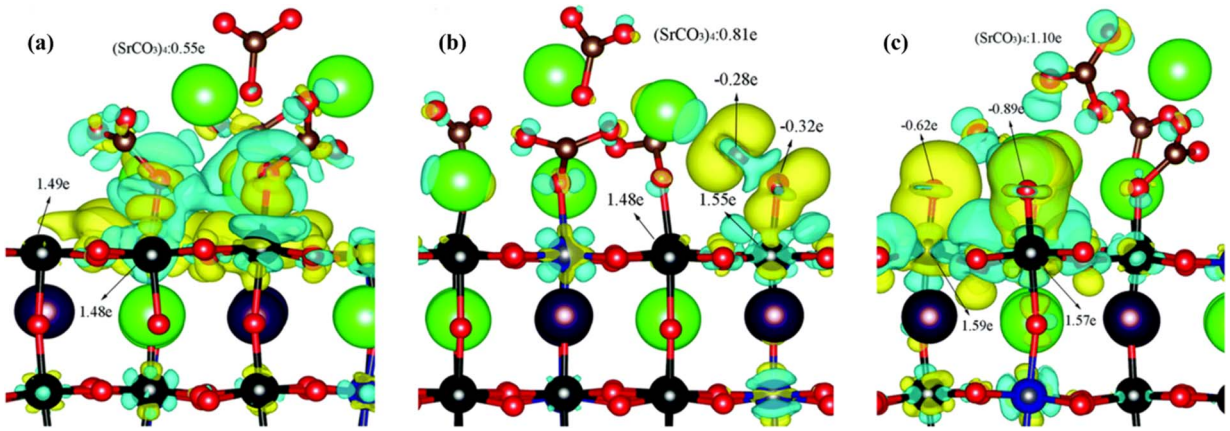

Fig. 12 Differential charge densities of (a) $SrCO_3$–LSCF, (b) O_2 adsorption, and (c) O_2 dissociation. Reproduced with permission.[152] Copyright 2017, Royal Society of Chemistry.

charges are enabled during oxygen adsorption (0.81*e*) and dissociation (1.10*e*) processes, suggesting the promotion effect of strontium carbonates on the ORR activity of the LSCF cathode. In a study by Han *et al.*, the adsorption selectivity of H_2O over CO_2 on various alkaline earth metal oxide surfaces was comparatively analysed using a simple gridding-based interpolation method.[180] Their results revealed that the BaO surface shows the highest surface-scale affinity for H_2O and CO_2. In contrast, the affinities of the SrO and CaO surfaces are relatively weaker, with MgO showcasing the lowest sensitivity of all. Additionally, working temperature and partial pressure are demonstrated to be of vital importance to surface adsorption selectivity. Such insights provide valuable guidance for revealing the complicated reaction mechanisms between contaminants and electrodes.

7. Challenges and perspectives

Based on the empirical analysis, a near-ideal CO_2-resistant perovskite cathode theoretically requires a sufficiently high acidity, in other words, a highly negative ABE. However, it remains uncertain whether such a methodology works or not under realistic conditions due to the complexity of the operating environment. The CO_2 resistance of perovskite cathodes is fundamentally governed by multiple aspects, including intrinsic properties (crystal structure, surface morphology, phase composition, *etc.*), as well as external conditions (working temperature, CO_2 partial pressure, exposure time, *etc.*). Achieving completely CO_2-tolerant perovskite cathodes is highly contingent on the rational integration of the aforementioned factors. To this end, continuous innovation and research are required to unravel the complexities and overcome the obstacles inherent in the development of CO_2-tolerant cathode materials.

Over the past several years, our group has deeply engaged in significant research endeavors, primarily focused on the performance optimization of perovskite ferrite cathodes. With an aim to reinforce the CO_2-resistance of the $BaFeO_3$ matrix, we implemented a co-doping strategy using high-acidity agents to develop a novel $Ba_{0.75}Sr_{0.25}Fe_{0.875}Y_{0.125}O_{3-\delta}$ (BSFY) cathode. This approach enables the BSFY electrode to showcase impressive CO_2-tolerance with an ultralow deterioration rate of $\sim$0.00011 Ω cm^2 min^{-1}, surpassing that of a great majority of reported CO_2-resistant perovskite analogues.[86] Seeking further enhancement, we formulated a composite cathode with a nominal composition of $Bi_{0.7}Pr_{0.1}Ba_{0.2}FeO_{3-\delta}$ (BPBF) and SDC for short-term contaminant poisoning tests. Encouragingly, the BPBF-based electrode performs stably with a constant electroactivity of 0.31 Ω cm^2 at 600 °C over a 50 h period, suggesting its significant potential as a practical air electrode material.[51] Apart from CO_2 resistance, electrode reversibility associated with operational durability is also of paramount importance. A portion of our research has been dedicated to probing the reversible effect of cathode materials at reduced temperatures, such as $Ba_{0.75}Sr_{0.25}Fe_{0.95}P_{0.05}O_{3-\delta}$,[63] $Ba_{0.95}Fe_{0.7}Co_{0.2}Sc_{0.1}O_{3-\delta}$,[64] and $Ba_{0.5}Sr_{0.5}Co_{0.7}Fe_{0.2}Ni_{0.1}O_{3-\delta}$.[114] Given the unclear structure–activity relationship in the presence of a contaminant, a more in-depth exploration is essential to accelerate the advancement of CO_2-tolerant cathodes.

As outlined above, there exist significant developmental gaps and future perspectives, summarized as follows:

(i) Need for efficient cathode materials with perfect CO_2-tolerance:

Low-temperature SOFCs operating below 500 °C are viewed as a more promising avenue toward commercialization, yet until now, there has been limited emphasis on developing robust air electrodes against gaseous contaminants at these temperatures. To meet the practical requirements, completely CO_2-tolerant cathodes for low-temperature operation are highly desired.

(ii) Turning CO_2 poisoning effects into benefits:

Contrary to traditional views, it is observed that a certain amount of carbonate precipitate is potentially of great benefit for the ORR activity of cathode materials.[158] Gu *et al.* also proposed that superior electrode performance could be achieved through surface self-reconstruction after CO_2 removal.[87] These benefits represent an emerging approach to design state-of-the-art cathode materials. To ensure the viability and

sustainability of SOFCs, such innovations deserve further exploration in future applications.

(iii) Deepening insights into structure–activity relationships:

The interaction mechanism between perovskite electrodes and gaseous pollutants under realistic operating conditions is still an unsolved issue in this domain. *In situ* and *operando* studies, proven as fruitful measurement tools, have provided more detailed insights into reaction processes. In response to the challenge, comprehensive utilization of *in situ* and *operando* techniques is essential to establish a set of systematic methodologies in terms of existing cases, so as to shed light on the structure–activity relationship toward efficient and durable cathode materials.

(iv) Accelerating development with a machine learning (ML)-assisted technique:

By deep learning methods with the integration of key properties (acidity, ABE, *etc.*), potential candidate materials can be effectively screened using artificial intelligence models. Conventional empirical experiments are generally time-consuming and cost-ineffective. Hence, the development of facile and reliable ML models with supervised learning algorithms is crucial for the rapid identification of highly CO_2-tolerant perovskite cathode materials.

In conclusion, optimizing the CO_2 tolerance of SOFC cathodes is a multifaceted challenge necessitating concerted efforts in theoretical analysis, experimental investigation, and advanced technology deployment. For one thing, prioritizing combined theoretical and experimental analysis is imperative for improving SOFC cathodes, and for another, more real-time, accurate, and sophisticated technologies also urgently need to be popularized for elucidating the structure–activity relationship and ensuring the reproducibility of experimental results. The insights and guidance provided in this review are intended to stimulate further research and innovation in this field, accelerating the realization of multi-functional SOFC air electrodes with perfect CO_2 resistance, thereby contributing to the advancement of sustainable energy solutions. While the journey may be long and fraught with challenges, the potential benefits in terms of energy efficiency, environmental sustainability, and industrial applicability are immense, making every effort in this direction worthwhile for meeting future energy demands.

Data availability

No primary research results, software or code have been included and no new data were generated or analysed as part of this review.

Conflicts of interest

There are no conflicts to declare.

Acknowledgements

This work was financially supported by the National Natural Science Foundation of China (No. 22108043) and Natural Science Foundation of Guangdong Province, China (No. 2023A1515012711).

References

1 F. Liu, H. Deng, D. Diercks, P. Kumar, M. H. A. Jabbar, C. Gumeci, Y. Furuya, N. Dale, T. Oku, M. Usuda, P. Kazempoor, L. Fang, D. Chen, B. Liu and C. Duan, *Nat. Energy*, 2023, **8**, 1145.
2 Z. Zhuang, Y. Li, R. Yu, L. Xia, J. Yang, Z. Lang, J. Zhu, J. Huang, J. Wang, Y. Wang, L. Fan, J. Wu, Y. Zhao, D. Wang and Y. Li, *Nat. Catal.*, 2022, **5**, 300.
3 Y. Wang, Y. Ling, B. Wang, G. Zhai, G. Yang, Z. Shao, R. Xiao and T. Li, *Energy Environ. Sci.*, 2023, **16**, 5721.
4 S. Koohfar, M. Ghasemi, T. Hafen, G. Dimitrakopoulos, D. Kim, J. Pike, S. Elangovan, E. D. Gomez and B. Yildiz, *Nat. Commun.*, 2023, **14**, 7203.
5 Z. Liu, Z. Tang, Y. Song, G. Yang, W. Qian, M. Yang, Y. Zhu, R. Ran, W. Wang, W. Zhou and Z. Shao, *Nano-Micro Lett.*, 2022, **14**, 217.
6 Y. Xia, Z. Jin, H. Wang, Z. Gong, H. Lv, R. Peng, W. Liu and L. Bi, *J. Mater. Chem. A*, 2019, **7**, 16136.
7 K. Pei, Y. Zhou, K. Xu, H. Zhang, Y. Ding, B. Zhao, W. Yuan, K. Sasaki, Y. Choi, Y. Chen and M. Liu, *Nat. Commun.*, 2022, **13**, 2207.
8 J. F. Shin, W. Xu, M. Zanella, K. Dawson, S. N. Savvin, J. B. Claridge and M. J. Rosseinsky, *Nat. Energy*, 2017, **2**, 16214.
9 N. N. M. Tahir, N. A. Baharuddin, A. A. Samat, N. Osman and M. R. Somalu, *J. Alloys Compd.*, 2022, **894**, 162458.
10 R. Zhou, Y. Yin, H. Dai, X. Yang, Y. Gu and L. Bi, *J. Adv. Ceram.*, 2023, **12**, 1189.
11 Y. Zhou, H. Wu, T. Luo, J. Wang, Y. Shi, C. Xia, S. Wang and Z. Zhan, *Adv. Energy Mater.*, 2015, **5**, 1500375.
12 L. Zhang, J. Shan and Q. Wang, *J. Alloys Compd.*, 2019, **771**, 221.
13 Y. Song, J. Liu, Y. Wang, D. Guan, A. Seong, M. Liang, M. J. Robson, X. Xiong, Z. Zhang, G. Kim, Z. Shao and F. Ciucci, *Adv. Energy Mater.*, 2021, **11**, 2101899.
14 J. M. Porras-Vazquez, T. F. Kemp, J. V. Hanna and P. R. Slater, *J. Mater. Chem.*, 2012, **22**, 8287.
15 A. Ndubuisi, S. Abouali, K. Singh and V. Thangadurai, *J. Mater. Chem. A*, 2022, **10**, 2196.
16 Y. Yin, Y. Zhou, Y. Gu and L. Bi, *J. Adv. Ceram.*, 2023, **12**, 587.
17 V. Cascos, L. Troncoso, A. L. Larralde, M. T. Fernandez-Diaz and J. A. Alonso, *ACS Appl. Energy Mater.*, 2020, **3**, 6709.
18 T. Sakai, M. Ogushi, K. Hosoi, A. Inoishi, H. Hagiwara, S. Ida, M. Oishi and T. Ishihara, *J. Mater. Chem. A*, 2021, **9**, 3584.
19 C. Zhao, N. Li, R. Zhang, Z. Zhu, J. Lin, K. Zhang and C. Zhao, *ACS Appl. Mater. Interfaces*, 2019, **11**, 47858.
20 C. Duan, D. Hook, Y. Chen, J. Tong and R. O'Hayre, *Energy Environ. Sci.*, 2017, **10**, 176.
21 K. T. Lee, A. A. Lidie, H. S. Yoon and E. D. Wachsman, *Angew. Chem., Int. Ed.*, 2014, **53**, 13463.
22 F. Dong, Y. Chen, D. Chen and Z. Shao, *ACS Appl. Mater. Interfaces*, 2014, **6**, 11180.

23 V. Cascos, L. Troncoso, A. Larralde, C. Álvarez-Galván, M. T. Fernandez-Díaz and J. A. Alonso, *ACS Appl. Energy Mater.*, 2020, **4**, 500.
24 F. Dong, Y. Chen, R. Ran, D. Chen, M. O. Tadé, S. Liu and Z. Shao, *J. Mater. Chem. A*, 2013, **1**, 9781.
25 N. Wang, S. Hinokuma, T. Ina, C. Zhu, H. Habazaki and Y. Aoki, *J. Mater. Chem. A*, 2020, **8**, 11043.
26 M. B. Hanif, M. Motola, S. qayyum, S. Rauf, A. khalid, C.-J. Li and C.-X. Li, *Chem. Eng. J.*, 2022, **428**, 132603.
27 R. V. Kumar and A. P. Khandale, *Renewable Sustainable Energy Rev.*, 2022, **156**, 111985.
28 J. Yi, M. Schroeder, T. Weirich and J. Mayer, *Chem. Mater.*, 2010, **22**, 6246.
29 J. Zhang, S. Ricote, P. V. Hendriksen and Y. Chen, *Adv. Funct. Mater.*, 2022, **32**, 2111205.
30 G. Yang, C. Su, H. Shi, Y. Zhu, Y. Song, W. Zhou and Z. Shao, *Energy Fuels*, 2020, **34**, 15169.
31 Z. Wei, Z. Li, Z. Wang, Y. Zhao, J. Wang and J. Chai, *Int. J. Hydrogen Energy*, 2022, **47**, 13490.
32 S. Sun and Z. Cheng, *J. Electrochem. Soc.*, 2016, **164**, F81.
33 J. Wang, Z. Yang, Y. Lv, F. Jiang, Y. Chen and S. Peng, *J. Electroanal. Chem.*, 2019, **847**, 113256.
34 Y. Zhu, W. Zhou, Y. Chen and Z. Shao, *Angew. Chem., Int. Ed.*, 2016, **55**, 8988.
35 Y. Chen, S. Yoo, Y. Choi, J. H. Kim, Y. Ding, K. Pei, R. Murphy, Y. Zhang, B. Zhao, W. Zhang, H. Chen, Y. Chen, W. Yuan, C. Yang and M. Liu, *Energy Environ. Sci.*, 2018, **11**, 2458.
36 C. Zhang, J. Sunarso and S. Liu, *Chem. Soc. Rev.*, 2017, **46**, 2941.
37 W. Xia, Q. Li, L. Sun, L. Huo and H. Zhao, *J. Alloys Compd.*, 2020, **835**, 155406.
38 X. Ding, Z. Gao, D. Ding, X. Zhao, H. Hou, S. Zhang and G. Yuan, *Appl. Catal., B*, 2019, **243**, 546.
39 S. Z. Golkhatmi, M. I. Asghar and P. D. Lund, *Renewable Sustainable Energy Rev.*, 2022, **161**, 112339.
40 F. Zhong, X. Wang, L. Wang, H. Fang, Y. Luo, C. Chen, L. Lin, D. Wang, K. Chen and L. Jiang, *Sep. Purif. Technol.*, 2023, **312**, 123397.
41 Y. Zhang, R. Knibbe, J. Sunarso, Y. Zhong, W. Zhou, Z. Shao and Z. Zhu, *Adv. Mater.*, 2017, **29**, 1770345.
42 Z. Li, M. Li and Z. Zhu, *Electrochem. Energy Rev.*, 2021, **5**, 263.
43 A. Aphale, C. Liang, B. Hu, and P. Singh, *Solid Oxide Fuel Cell Lifetime Reliab.*, 2017, p. 101.
44 G. Li, H. Jin, L. Gui, B. He and L. Zhao, *Int. J. Hydrogen Energy*, 2018, **43**, 3291.
45 H. Gu, C. Su, C. Zhou, Y. Liu, Y. Zhang, G. Yang, W. Zhou and Z. Shao, *Int. J. Hydrogen Energy*, 2022, **47**, 16214.
46 H. Qi, Z. Zhao, B. Tu and M. Cheng, *J. Power Sources*, 2020, **455**, 227971.
47 W. Yi, Y. Tian, C. Lu, B. Wang, Y. Liu, S. Gao and B. Niu, *J. Eur. Ceram. Soc.*, 2022, **42**, 2860.
48 F. Bu, F. Yang, Y. He, M. Wang, Y. Li and Q. Zhou, *Mater. Res. Bull.*, 2022, **146**, 111624.
49 D. Wang, Y. Xia, H. Lv, L. Miao, L. Bi and W. Liu, *Int. J. Hydrogen Energy*, 2020, **45**, 31017.
50 A. U. Rehman, M. Li, R. Knibbe, M. S. Khan, V. K. Peterson, H. E. A. Brand, Z. Li, W. Zhou and Z. Zhu, *ACS Appl. Mater. Interfaces*, 2019, **11**, 26909.
51 L. Li, Z. Kong, B. Yao, H. Yang, Z. Gao, L. Xu, F. Dong, M. Ni and Z. Lin, *Chem. Eng. J.*, 2020, **396**, 125237.
52 C. Xu, K. Sun, X. Yang, M. Ma, R. Ren, J. Qiao, Z. Wang, S. Zhen and W. Sun, *J. Power Sources*, 2020, **450**, 227722.
53 J. Li, Z. Gao, H. Min, M. Li, Y. Lu, X. Wang and X. Ding, *J. Power Sources*, 2021, **506**, 230057.
54 D. Huan, L. Zhang, K. Zhu, X. Li, N. Shi, Y. Yang, C. Xia, Y. Xie and R. Peng, *J. Power Sources*, 2021, **497**, 229872.
55 N. Han, R. Ren, M. Ma, C. Xu, J. Qiao, W. Sun, K. Sun and Z. Wang, *Chin. Chem. Lett.*, 2022, **33**, 2658.
56 X. Lv, H. Chen, W. Zhou, S.-D. Li, F. Cheng and Z. Shao, *Renewable Energy*, 2022, **185**, 8.
57 Y. Liu, Y. Cao, S. Sun, C. Lu, B. Wang, G. Liu, S. Gao and B. Niu, *J. Eur. Ceram. Soc.*, 2023, **43**, 1028.
58 Z. Yang, T. Xia, Z. Dong, Q. Li, L. Sun, L. Huo and H. Zhao, *Sep. Purif. Technol.*, 2023, **317**, 123936.
59 F. He, F. Zhu, K. Xu, Y. Xu, D. Liu, G. Yang, K. Sasaki, Y. Choi and Y. Chen, *Appl. Catal., B*, 2024, **355**, 124175.
60 B. Xia, H. Zhang, C. Yao, H. Lou, M. Chen, Z. Zhang, Y. Sun, W. Zhang, H. Wang, X. Lang and K. Cai, *Appl. Surf. Sci.*, 2024, **649**, 159143.
61 J.-W. Yin, C. Zhang, Y.-M. Yin, H. Shi, Y. Lin, J. Lu and Z.-F. Ma, *J. Power Sources*, 2015, **286**, 217.
62 Y. Zhang, G. Yang, G. Chen, R. Ran, W. Zhou and Z. Shao, *ACS Appl. Mater. Interfaces*, 2016, **8**, 3003.
63 F. Dong, Z. Ma, Q. Ye, B. Zhang, L. Li, G. Yang, M. Ni and Z. Lin, *Small Methods*, 2022, **6**, 2200292.
64 Z. Ma, Q. Ye, B. Zhang, W. Yang, F. Dong, M. Ni and Z. Lin, *Adv. Funct. Mater.*, 2022, **32**, 2209054.
65 Y. Zhu, Z. G. Chen, W. Zhou, S. Jiang, J. Zou and Z. Shao, *ChemSusChem*, 2013, **6**, 2249.
66 T. Yang, C. Su, W. Wang, L. Meng, J. Deng, Y. Liu, S. S. Rathore and Z. Shao, *Appl. Surf. Sci.*, 2019, **472**, 10.
67 J. Wang, Z. Yang, L. Ba, Y. Chen, B. Ge and S. Peng, *J. Electroanal. Chem.*, 2018, **827**, 79.
68 P. Qiu, A. Wang, J. Li, Z. Li, L. Jia, B. Chi, J. Pu and J. Li, *J. Power Sources*, 2016, **327**, 408.
69 W. Xia, Q. Li, L. Sun, L. Huo and H. Zhao, *J. Eur. Ceram. Soc.*, 2020, **40**, 1967.
70 Y. Gou, G. Li, R. Ren, C. Xu, J. Qiao, W. Sun, K. Sun and Z. Wang, *ACS Appl. Mater. Interfaces*, 2021, **13**, 20174.
71 J. Gao, Q. Li, W. Xia, L. Sun, L.-H. Huo and H. Zhao, *ACS Sustainable Chem. Eng.*, 2019, **7**, 18647.
72 J. Druce, H. Téllez and J. Hyodo, *MRS Bull.*, 2014, **39**, 810.
73 D. J. Deka, J. Kim, S. Gunduz, D. Jain, Y. Shi, J. T. Miller, A. C. Co and U. S. Ozkan, *Appl. Catal., B*, 2021, **283**, 119642.
74 Y. Xu, X. Xu and L. Bi, *J. Adv. Ceram.*, 2022, **11**, 794.
75 E. Ostrovskiy, Y.-L. Huang and E. D. Wachsman, *J. Mater. Chem. A*, 2021, **9**, 1593.
76 J. Li, J. Hou, Y. Lu, Q. Wang, X. Xi, Y. Fan, X.-Z. Fu and J.-L. Luo, *J. Power Sources*, 2020, **453**, 227909.
77 L. Shen, Z. Du, Y. Zhang, X. Dong and H. Zhao, *Appl. Catal., B*, 2021, **295**, 120264.

78 Q. Yang, D. Tian, R. Liu, H. Wu, Y. Chen, Y. Ding, X. Lu and B. Lin, *Int. J. Hydrogen Energy*, 2021, **46**, 5630.
79 Z. Wang, J. Li, M. Yuan, J. Gao, H. Hao, A. M. Abdalla, L. Xu, Z. Lv and B. Wei, *Sustainable Mater. Technol.*, 2024, **40**, e00969.
80 N. C. Jeong, J. S. Lee, E. L. Tae, Y. J. Lee and K. B. Yoon, *Angew. Chem., Int. Ed.*, 2008, **47**, 10128.
81 L. Gao, Q. Li, L. Sun, T. Xia, L. Huo, H. Zhao and J.-C. Grenier, *J. Mater. Chem. A*, 2018, **6**, 15221.
82 X. Hu, Y. Xie, Y. Wan, Y. Yang, X. Wu and C. Xia, *Appl. Catal., B*, 2021, **286**, 119901.
83 Z. Han, J. Bai, X. Chen, X. Zhu and D. Zhou, *Int. J. Hydrogen Energy*, 2021, **46**, 11894.
84 L. Shao, F. Si, X.-Z. Fu and J.-L. Luo, *Int. J. Hydrogen Energy*, 2018, **43**, 7511.
85 Y. Zhang, X. Gao, J. Sunarso, B. Liu, W. Zhou, M. Ni and Z. Shao, *ACS Appl. Energy Mater.*, 2018, **1**, 1337.
86 Z. Ma, L. Li, Q. Ye, B. Dongyang, W. Yang, F. Dong and Z. Lin, *ACS Appl. Mater. Interfaces*, 2022, **14**, 30881.
87 H. Gu, J. Sunarso, G. Yang, C. Zhou, Y. Song, Y. Zhang, W. Wang, R. Ran, W. Zhou and Z. Shao, *ACS Appl. Mater. Interfaces*, 2020, **12**, 16417.
88 J. Zhang, X. Li, Z. Zhang, X. Xu, Y. Chen, Y. Song, J. Dai, G. Yang, R. Ran, W. Zhou and Z. Shao, *J. Power Sources*, 2020, **457**, 227995.
89 T. Su, T. Zhang, H. Xie, J. Zhong and C. Xia, *Int. J. Hydrogen Energy*, 2022, **47**, 16272.
90 Z. Sun, Z. Liu, C. Cai, H. Deng, F. Yang, Y. Lu, X. Song, S. An and H. Zhao, *Sep. Purif. Technol.*, 2022, **289**, 120742.
91 D. Zou, Y. Yi, Y. Song, D. Guan, M. Xu, R. Ran, W. Wang, W. Zhou and Z. Shao, *J. Mater. Chem. A*, 2022, **10**, 5381.
92 L. Xing, T. Xia, Q. Li, H. Zhao, L. Sun and L.-H. Huo, *ACS Sustainable Chem. Eng.*, 2019, **7**, 17907.
93 Y. Meng, L. Sun, J. Gao, W. Tan, C. Chen, J. Yi, H. J. M. Bouwmeester, Z. Sun and K. S. Brinkman, *ACS Appl. Mater. Interfaces*, 2019, **11**, 11498.
94 B. Liu, N. Li, L. Sun, Q. Li, L. Huo and H. Zhao, *J. Alloys Compd.*, 2021, **870**, 159397.
95 J. Gao, Q. Li, L. Sun, L. Huo and H. Zhao, *Ceram. Int.*, 2019, **45**, 20226.
96 M. Guo, Q. Li, J. Gao, L. Sun, L. Huo and H. Zhao, *J. Alloys Compd.*, 2021, **858**, 158265.
97 Y. Zhu, J. Sunarso, W. Zhou and Z. Shao, *Appl. Catal., B*, 2015, **172**, 52.
98 Z. Zhang, D. Chen, J. Wang, S. Tan, X. Yu and Z. Shao, *ACS Appl. Energy Mater.*, 2018, **1**, 2134.
99 X. Zhang, T. Xia, Q. Li, L. Sun, L. Huo and H. Zhao, *J. Alloys Compd.*, 2021, **858**, 157743.
100 L. Zhu, B. Wei, Z. Lü, J. Feng, L. Xu, H. Gao, Y. Zhang and X. Huang, *Appl. Surf. Sci.*, 2017, **416**, 649.
101 L. Almar, H. Störmer, M. Meffert, J. Szász, F. Wankmüller, D. Gerthsen and E. Ivers-Tiffée, *ACS Appl. Energy Mater.*, 2018, **1**, 1316.
102 J. Li, X. Zhao, H. Min, Y. Lu, M. Li and X. Ding, *Int. J. Hydrogen Energy*, 2020, **45**, 31070.
103 M. Li, X. Zhao, H. Min, G. Yuan and X. Ding, *Int. J. Hydrogen Energy*, 2020, **45**, 34058.
104 M. Guo, T. Xia, Q. Li, L. Sun and H. Zhao, *J. Eur. Ceram. Soc.*, 2021, **41**, 6531.
105 J. Gao, D. Ma, H. Zhao, Q. Li, Z. Lü and B. Wei, *Energy*, 2022, **252**, 124050.
106 J. Li, Q. Zhang, P. Qiu, L. Jia, B. Chi, J. Pu and J. Li, *J. Power Sources*, 2017, **342**, 623.
107 F. Lu, T. Xia, Q. Li, J. Wang, L. Huo and H. Zhao, *Appl. Catal., B*, 2019, **249**, 19.
108 F. Lu, T. Xia, Q. Li, L. Sun, L. Huo and H. Zhao, *J. Power Sources*, 2019, **417**, 42.
109 Y. Lu, L. Ding, M. Li, J. Li, X. Wang and X. Ding, *Electrochim. Acta*, 2021, **398**, 139323.
110 S. Lü, Y. Zhu, X. Fu, R. Huang, Y. Guo, W. Zhang, H. Li, L. Hou and X. Meng, *J. Alloys Compd.*, 2022, **911**, 165002.
111 M. Li, W. Zhou and Z. Zhu, *ACS Appl. Mater. Interfaces*, 2017, **9**, 2326.
112 G. Yang, C. Su, Y. Chen, F. Dong, M. O. Tade and Z. Shao, *J. Eur. Ceram. Soc.*, 2015, **35**, 2531.
113 Y. Zhu, W. Zhou, R. Ran, Y. Chen, Z. Shao and M. Liu, *Nano Lett.*, 2016, **16**, 512.
114 L. Li, H. Yang, Z. Gao, Y. Zhang, F. Dong, G. Yang, M. Ni and Z. Lin, *J. Mater. Chem. A*, 2019, **7**, 12343.
115 X. Liu, F. Jin, X. Liu, N. Sun, J. Li, Y. Shen, F. Wang, L. Yang, X. Chu, M. Xu, Y. Zhai and J. Li, *Electrochim. Acta*, 2021, **390**, 138830.
116 H. Wang, W. Zhang, K. Guan, Z. Wei, J. Meng, J. Meng and X. Liu, *ACS Sustainable Chem. Eng.*, 2020, **8**, 3367.
117 Y. Bu, Q. Zhong, D.-C. Chen, Y. Chen, S. Y. Lai, T. Wei, H. Sun, D. Ding and M. Liu, *J. Power Sources*, 2016, **319**, 178.
118 Y. S. Kim and S. G. Kang, *Appl. Surf. Sci.*, 2019, **486**, 571.
119 S. Wu, X. Xu, X. Li and L. Bi, *Sci. China Mater.*, 2021, **65**, 675.
120 X. Lu, X. Yang, L. Jia, B. Chi, J. Pu and J. Li, *Int. J. Hydrogen Energy*, 2019, **44**, 16359.
121 K. Pei, Y. Zhou, Y. Ding, K. Xu, H. Zhang, W. Yuan, K. Sasaki, Y. Choi, M. Liu and Y. Chen, *J. Power Sources*, 2021, **514**, 230573.
122 Q. Zeng, Y. Zuo, C. Fan and C. Chen, *J. Membr. Sci.*, 2009, **335**, 140.
123 F. Wang, X. Xu, Y. Xia, B. Dong, N. Ke, L. Hao, L. Bi, X. Xu and W. Liu, *Int. J. Hydrogen Energy*, 2021, **46**, 33561.
124 D. Ma, J. Gao, T. Xia, Q. Li, L. Sun, L. Huo and H. Zhao, *Coatings*, 2020, **10**, 1260.
125 M. Li, H. Niu, J. Druce, H. Téllez, T. Ishihara, J. A. Kilner, H. Gasparyan, M. J. Pitcher, W. Xu, J. F. Shin, L. M. Daniels, L. A. H. Jones, V. R. Dhanak, D. Hu, M. Zanella, J. B. Claridge and M. J. Rosseinsky, *Adv. Mater.*, 2019, **32**, 1905200.
126 K.-Y. Lai and A. Manthiram, *J. Mater. Chem. A*, 2019, **7**, 8540.
127 Y. Gao, X. Huang, M. Yuan, J. Gao, Z. Wang, A. M. Abdalla, A. K. Azad, L. Xu, Z. Lv and B. Wei, *J. Power Sources*, 2022, **540**, 231661.
128 X. Ding, M. Li, X. Zhao, L. Ding, Y. Yan, L. Wang and Z. Wang, *Sustainable Energy Fuels*, 2020, **4**, 1168.
129 K. Shi, Y. Yin, Z. Tang, S. Yu and Q. Zhang, *Ceram. Int.*, 2022, **48**, 13024.
130 H. Hu, Y. Lu, X. Zhou, J. Li, X. Wang and X. Ding, *J. Power Sources*, 2022, **548**, 232049.

131 A. I. Klyndyuk, E. A. Chizhova, D. S. Kharytonau and D. A. Medvedev, *Materials*, 2021, **15**, 141.
132 Y. Lu, X. Zhao, Z. Wang and X. Ding, *Sustainable Energy Fuels*, 2020, **4**, 5229.
133 S. Yu, X. Yang, Y. Wang and L. Bi, *Ceram. Int.*, 2022, **48**, 28751.
134 A. Samreen, M. S. Ali, M. Huzaifa, N. Ali, B. Hassan, F. Ullah, S. Ali and N. A. Arifin, *Chem. Rec.*, 2024, **24**, e202300247.
135 L. Zhang, Y. Yin, Y. Xu, S. Yu and L. Bi, *Sci. China Mater.*, 2022, **65**, 1485.
136 J. Gao, Y. Liu, Y. Gao, M. Yuan, Z. Wang, Z. Lü, Q. Li and B. Wei, *Chem. Eng. J.*, 2023, **452**, 139584.
137 Y. Yin, H. Dai, S. Yu, L. Bi and E. Traversa, *SusMat*, 2022, **2**, 607.
138 M. Su, D. Huan, X. Hu, K. Zhu, R. Peng and C. Xia, *J. Power Sources*, 2022, **521**, 230907.
139 G. Jeerh, M. Zhang and S. Tao, *J. Mater. Chem. A*, 2021, **9**, 727.
140 S. Peng, S. Lei, S. Wen, J. Xue and H. Wang, *Chin. J. Chem. Eng.*, 2023, **56**, 25.
141 Y. Yin, D. Xiao, S. Wu, E. H. Da'as, Y. Gu and L. Bi, *SusMat*, 2023, **3**, 697.
142 J. Hou, L. Miao, J. Hui, L. Bi, W. Liu and J. T. S. Irvine, *J. Mater. Chem. A*, 2018, **6**, 10411.
143 H. Dai, Y. Yin, X. Li, C. Ma, Z. Chen, M. Hua and L. Bi, *Sustainable Mater. Technol.*, 2022, **32**, e00409.
144 H. Dai, X. Xu, C. Liu, C. Ma, Q. Zhang and L. Bi, *J. Mater. Chem. A*, 2021, **9**, 12553.
145 S. Darvish, M. Asadikiya, B. Hu, P. Singh and Y. Zhong, *Int. J. Hydrogen Energy*, 2016, **41**, 10239.
146 S. He, Y. Yin, L. Bi and H. Dai, *Ceram. Int.*, 2022, **48**, 11872.
147 J.-H. Zhang, F.-Z. Han, C.-X. Li and S.-L. Zhang, *J. Eur. Ceram. Soc.*, 2022, **42**, 5801.
148 S. He, H. Dai and L. Bi, *Ceram. Int.*, 2022, **48**, 35586.
149 E. Y. Konysheva, X. Xu and J. T. S. Irvine, *Adv. Mater.*, 2011, **24**, 528.
150 Q. Ye, H. Ye, Z. Ma, H. Lin, B. Zhao, G. Yang, F. Dong, M. Ni, Z. Lin and S. Zhang, *Small*, 2024, 2307900.
151 H. Lv, L. Lin, X. Zhang, R. Li, Y. Song, H. Matsumoto, N. Ta, C. Zeng, Q. Fu, G. Wang and X. Bao, *Nat. Commun.*, 2021, **12**, 5665.
152 X. Xi, Y. Fan, J. Zhang, J.-L. Luo and X.-Z. Fu, *J. Mater. Chem. A*, 2022, **10**, 2509.
153 D. Ding, X. Li, S. Y. Lai, K. Gerdes and M. Liu, *Energy Environ. Sci.*, 2014, **7**, 552.
154 M. Liu, D. Ding, K. Blinn, X. Li, L. Nie and M. Liu, *Int. J. Hydrogen Energy*, 2012, **37**, 8613.
155 F. Du, W. Sun, H. Luo and C. M. Li, *Mater. Rep.: Energy*, 2022, **2**, 100163.
156 D. Ding, M. Liu, Z. Liu, X. Li, K. Blinn, X. Zhu and M. Liu, *Adv. Energy Mater.*, 2013, **3**, 1149.
157 P. Qiu, X. Yang, T. Zhu, S. Sun, L. Jia and J. Li, *Int. J. Hydrogen Energy*, 2020, **45**, 23160.
158 M. Li, Z. Sun, W. Yang, T. Hong, Z. Zhu, Y. Zhang, X. Wu and C. Xia, *Phys. Chem. Chem. Phys.*, 2017, **19**, 503.
159 B. Gu, J. Sunarso, Y. Zhang, Y. Song, G. Yang, W. Zhou and Z. Shao, *J. Power Sources*, 2018, **405**, 124.
160 Y. Bu, S. Joo, Y. Zhang, Y. Wang, D. Meng, X. Ge and G. Kim, *J. Power Sources*, 2020, **451**, 227812.
161 A. Giuliano, M. P. Carpanese, M. Panizza, G. Cerisola, D. Clematis and A. Barbucci, *Electrochim. Acta*, 2017, **240**, 258.
162 E. A. Antipinskaya, B. V. Politov, D. A. Osinkin, A. Y. Suntsov and V. L. Kozhevnikov, *Electrochim. Acta*, 2021, **365**, 137372.
163 K. Wu, L. Fu, J. Zhou, L. Zhou, J. Yang, Z. Liu, H. Zhao, Q. Deng and K. Wu, *Ceram. Int.*, 2023, **49**, 9848.
164 K. Yang, Y. Wang, Z. Yang, Y. Wang and C. Jin, *Int. J. Hydrogen Energy*, 2020, **45**, 34080.
165 Y. Jing, X. Zhou, P. Lund, C. Chen and L. Fan, *Int. J. Hydrogen Energy*, 2021, **46**, 9898.
166 M. Wang, R. Qian, M. Bao, C. Gu and P. Zhu, *Mater. Lett.*, 2018, **210**, 203.
167 M. Mohsin, A. Yousaf, R. Raza and R. Zia, *J. Alloys Compd.*, 2019, **791**, 248.
168 A. Cavalli, P. Chundru, T. Brunner, I. Obernberger, I. Mirabelli, R. Makkus and P. V. Aravind, *Renewable Energy*, 2021, **180**, 673.
169 Z. Arab Aboosadi and M. Farhadi Yadecoury, *Int. J. Chem. React. Eng.*, 2019, **17**, 20190108.
170 S. Faraji, K. J. Nordheden and S. M. Stagg-Williams, *Appl. Catal., B*, 2010, **99**, 118.
171 C. S. Shenoy, S. S. Patil, P. Govardhan, A. Shourya, H. P. Dasari, M. B. Saidutta and H. Dasari, *Emiss. Control Sci. Technol.*, 2019, **5**, 342.
172 S. Gangopadhayay, T. Inerbaev, A. E. Masunov, D. Altilio and N. Orlovskaya, *ACS Appl. Mater. Interfaces*, 2009, **1**, 1512.
173 C. Chatzichristodoulou, B. C. Hauback and P. V. Hendriksen, *J. Solid State Chem.*, 2013, **201**, 164.
174 M. Niania, R. Podor, T. B. Britton, C. Li, S. J. Cooper, N. Svetkov, S. Skinner and J. Kilner, *J. Mater. Chem. A*, 2018, **6**, 14120.
175 Y. Yu, A. Y. Nikiforov, T. C. Kaspar, J. C. Woicik, K. F. Ludwig, S. Gopalan, U. B. Pal and S. N. Basu, *J. Power Sources*, 2016, **333**, 247.
176 E. Sarnello, Z. Lu, S. Seifert, R. E. Winans and T. Li, *ACS Catal.*, 2021, **11**, 2605.
177 K. S. Adarsh, N. Chandrasekaran and V. Chakrapani, *Front. Chem.*, 2020, **8**, 137.
178 S. Y. Lai, D. Ding, M. Liu, M. Liu and F. M. Alamgir, *ChemSusChem*, 2014, **7**, 3078.
179 Z. Tao, X. Xu and L. Bi, *Electrochem. Commun.*, 2021, **129**, 107072.
180 Z. Han, Y. Yang and D. Kong, *Appl. Surf. Sci.*, 2020, **503**, 144333.
181 D. Huan, L. Zhang, K. Zhu, X. Li, B. Zhang, J. Shi, R. Peng and C. Xia, *Sep. Purif. Technol.*, 2022, **290**, 120843.